Synergistic effect of fibres on the physical, mechanical, and microstructural properties of aerogel-based thermal insulating renders

M. Pedroso[1], I. Flores-Colen[2], J. D. Silvestre[3], M. Glória Gomes[4], A. Hawreen[5, 6, 7*], R. J. Ball[8]

[1,]CERIS, DECivil, IST, Universidade de Lisboa, Av. Rovisco Pais, 1049-001 Lisbon, Portugal; email: marco.pedroso@tecnico.ulisboa.pt

[2] CERIS, DECivil, IST, Universidade de Lisboa, Av. Rovisco Pais, 1049-001 Lisbon, Portugal; email: ines.flores.colen@tecnico.ulisboa.pt

[3] CERIS, DECivil, IST, Universidade de Lisboa, Av. Rovisco Pais, 1049-001 Lisbon, Portugal; email: jose.silvestre@tecnico.ulisboa.pt

[4] CERIS, DECivil, IST, Universidade de Lisboa, Av. Rovisco Pais, 1049-001 Lisbon, Portugal; email: maria.gloria.gomes@tecnico.ulisboa.pt

[5] Department of Highway and Bridge Engineering, Technical Engineering College, Erbil Polytechnic University, Erbil 44001, Iraq

[6] Department of Civil Engineering, College of Engineering, Nawroz University, Duhok 42001, Iraq

[7] Universidade de Lisboa, IST, Av. Rovisco Pais, 1049-001 Lisbon, Portugal; hawreen.a@gmail.com,

[8] Department of Architecture and Civil Engineering, University of Bath, Bath BA2 7AY, United Kingdom; email: r.j.ball@bath.ac.uk * Corresponding authors: A. Hawreen

Abstract

There is an increasing demand for highly efficient thermal insulating materials in buildings. This study presents a novel solution incorporating nanomaterials, such as silica aerogel, which can achieve low thermal conductivity values (below 0.030 W m^{-1} K^{-1}) in renders. A key challenge of using aerogels is their low mechanical strength and high capillary water absorption. Here we describe a novel approach employing fibres which mitigates against some key properties which are decreased as a consequence of using aerogel. The incorporation of aramid (0.50%), sisal (0.10%), and biomass (0.10%) fibres (by total volume) was evaluated experimentally in terms of physical, mechanical, and microstructural properties. A synergistic effect between the fibres and aerogel increased mechanical resistance and a reduction in the capillary water absorption, when compared to the reference render (without fibres), whilst maintaining the low thermal conductivity. However, these properties depended significantly on whether the fibres were synthetic or organic. This study is important as it demonstrates that aerogel-based fibre-enhanced thermal renders can contribute to higher energy efficiency in both new construction and retrofitting. The use of these materials will have a direct positive impact on addressing the climate crisis.

Keywords: Energy-efficient buildings, Fibres, Nanomaterials, Performance, Silica aerogel, Thermal render

Abbreviations

DI - Drying index

DRIFT - Diffuse reflectance

DVS - Dynamic vapour sorption

EU - European Union

FTIR - Fourier transform infrared spectroscopy

ITZ - Interfacial transition zone

MIP - Mercury intrusion porosimeter

OM - Optical magnifier

RH - Relative humidity

SEM - Scanning electron microscope

TR - Thermal render

1. Introduction

In the European Union (EU), there is an increasing demand for energy and environmental directives applied to buildings, either in their construction or retrofitting [1,2]. This derives from the fact that 35% of the buildings are over 50 years old and almost 75% are energy inefficient [3]. These factors are associated to make the built environment climate-neutral by 2050, in line with the Paris Agreement [4], and that has to be achieved by both the use of innovative materials and energy consumption reduction.

One of the most effective ways of improving the energy efficiency of buildings is using thermal insulating materials on their envelope [5–8] since up to 80% of heat losses through walls and roofs occur through these elements [9–11]. This has led to the increase in thermal insulation demands applied to buildings by the EU regulations [1,2], promoting the development and application of innovative multifunctional materials [12,13] with high thermal insulating capabilities [14].

Several thermal insulating solutions have been used in the last few years for application on walls, with the adoption of low thermal conductivity materials being the main followed path [14,15]. The use of those solutions has contributed to improving the buildings' energy efficiency (reducing impacts), as they reduce application thicknesses while keeping high thermal insulation and, at the same time, improving the user's indoor comfort [15].

One of the most used solutions has been the External Thermal Insulation Composite System (ETICS) [16] since it combines different layers of materials with thermal insulating properties while also offering physical and mechanical protection. This preference can be related to their higher availability and low thermal conductivity (*e.g.* ETICS with EPS show values of $\lambda = 0.032$ W m^{-1} K^{-1} [17]). Nonetheless, they present some drawbacks: reduced water vapour diffusion; high fire reaction; difficulty in applying them on uneven surfaces; among others.

To improve some of those aspects, renders with improved thermal characteristics started to be applied on walls [18], typical thickness below 55 mm but depending on thermal requirements and climate zones, with the possibility to present some advantages over the ETICS: lower fire reaction; the potential for being applied directly over the substrate; but also the potential for being applied using mechanical projection machines, improving their applicability over irregular surfaces or architectural details [19,20]. However, these thermal renders (renders with a thermal conductivity ≤ 0.200 W m^{-1} K^{-1} according to the EN 998-1 [21]) still present high thermal conductivity values (conventional thermal renders which incorporate EPS or expanded cork granules), usually $\lambda \geq 0.050$ W m^{-1} K^{-1} [22]. Therefore, to benefit from the identified advantages of the thermal renders, while also promoting a lower thermal conductivity, more in line with the classic thermal insulating materials, and consequently, with higher energy efficiency, several nanomaterials have been incorporated in these renders, such as the silica aerogel granules [23–27].

However, the use of such nanomaterial presented some known problems, such as the difficulty of granules dispersion within the matrices, and their mechanical fragility [28–31], compromising the mechanical performance of the renders [32–34]. With further research, the granules' dispersion problem was partially solved by developing a new aerogel-based thermal insulating render [35,36]. Due to admixtures and a compatible binder matrix, it was possible to achieve a good aerogel dispersion while maintaining its shape integrity and render workability.

Although it was possible to lower the thermal conductivity (λ, for 10 ºC and dry-state) to values around 0.029 W m^{-1} K^{-1}, and to obtain a suitable water vapour diffusion resistance coefficient ($\mu = 14.8 \leq 15$), both compressive strength (≈ 45% lower than the declared values of commercially available thermal renders [18,37]) and the coefficient of capillary water absorption (≈ 100% higher than the standard requirements [23,38]) did not fulfil the EN 998-1 [21] requirements. To solve the mentioned problems, a protective coating system is applied over the render surface [39], which allows for improvement in the superficial impact resistance while lowering the capillary water absorption to values more in line with the ETAG 004 requirements, [40] now superseded by EAD 04008300-0404.

Based upon the research where it was seen that fibres have improved cement-based materials for several years [41,42], such as flexural strength and crack and shrinkage reduction [43–45], and also significantly improve the compressive strength [12,44] - fibre were herein incorporated to improve aerogel-based thermal render mechanical performance. In general, fibres mainly provide a stabilizing effect on the fracture process. Since natural fibres are

increasingly used due to sustainability concerns, they were the basis of this research, with the findings presented by Pedroso and Flores-Colen [12] guiding the choice of their best potential quantities and dimensions.

As the available literature investigating fibres' inclusion into thermal insulating renders is scarce and only considers a limited number of fibre types [33,46], this study was designed. The study used the aerogel-based thermal render previously developed by Pedroso *et al.* [35] as a reference (a blend of mineral binders, rheological and hydrophobic agents, resins, and lightweight and thermal insulating aggregates), while also testing powdered render replacements of synthetic and natural fibres to evaluate possible performance improvements over mechanical, physical and microstructural aspects. Since lower fibre dimensions and volume fractions could be associated with the improvement of the mechanical performance of cement-based composites [12], those guidelines were followed while incorporating different fibres in the aerogel-based thermal render during a preliminary campaign (presented in the *Supplementary data*).

When searching for the synthetic fibres to use, it was seen that aramid fibres have been presenting interesting results in improving the compressive and flexural strengths of cement-based composites [47,48], almost 50% in both cases, when compared with the reference. Therefore, synthetic fibre was one of the chosen materials in this study. Another fibre initially considered was of polypropylene origin, as it is also a widely used and available fibre [33,49,50]. These fibres followed the same guidelines applied to the natural fibres (quantities and dimensions) to allow a performance comparison.

For the natural plant-based fibres, one of the chosen was from sisal origin, collected from the plant leaves. This choice was also related to their availability, widespread use in concrete and mortars, and due to extensive published research with mechanical performance improvements reported, mainly on flexural characteristics [12,51,52], where it can improve up to 20% over the reference values. The other chosen fibre has its origin in the forest's biomass, resulting from leaves that stay behind after the pruning and cutting of the trees in the Portuguese forests of *Pinus pinaster*. The fibres' isolation is achieved following a process patented by the first author and another researcher [53]. Due to its novelty, no other works study its performance or incorporation in renders, where this material can represent an interesting added value to the forest economy. Therefore, it is essential to study its viability to be incorporated into construction materials.

Following the results from previous research [12,54] and the preliminary campaign (presented in the supplementary material, attached to this manuscript), a more in-depth experimental campaign was carried out using

substitutions of the powdered reference render [35]. The following volume fractions were selected to produce the thermal renders (TR): 0.50% (vol.) aramid – TR aramid; 0.10% (vol.) sisal – TR sisal; and 0.10% (vol.) biomass fibres – TR biomass; while a mixture without fibres was also produced (TR reference) for comparison purposes. These mixtures were considered the most significant based on their preliminary campaign test results (mechanical and physical) carried out for different fibre volumes (0.10%; 0.25%; 0.50%; 1.00% and 2.00%). These results are presented in the *Supplementary data*

Therefore, to evaluate the fibres' potential synergistic effect on the aerogel-based TR properties, an extensive laboratory campaign was carried out. This campaign intended to characterise the fibres and the composites' fresh formulation.

2.1. Materials

An aerogel-based TR was used that was developed in a previous study [35], with its formulation being mainly composed of a blend of mineral binders, rheological and hydrophobic agents, resins, and incorporating, as lightweight and thermal insulating aggregate, a commercially available supercritical silica aerogel in the form of granules (diameter ≤ 3500 μm, bulk density ≤ 90 kg m^{-3}, compressive strength ≤ 0.80 MPa, and a thermal conductivity ≤ 0.020 W m^{-1} K^{-1} [55]. In this render formulation, the silica aerogel granules represent the main material, occupying ≈ 70% (vol.). In the render powder (with a density of 135 kg m^{-3}), mineral binders (Portland cement and calcium aluminate cement) represented a total of 20 % (m/m), and silica aerogel hydrophobic granules a total of ~ 37 % (m/m), with the remaining quantities allocated to other components.

The chosen fibres were of two different origins: human-made (synthetic) and natural (plant). The synthetic fibres were Poly (p-phenylene terephthalamide), with the trade name of *Aramid roving 805 TEX* by *Twaron* [56] (Figure 1 a)). For the natural plant-based fibres, sisal (Figure 1 b)) and a new type of fibres derived from biomass waste that remains in the forest after cutting the trees (Figure 1 c)), were the ones used.

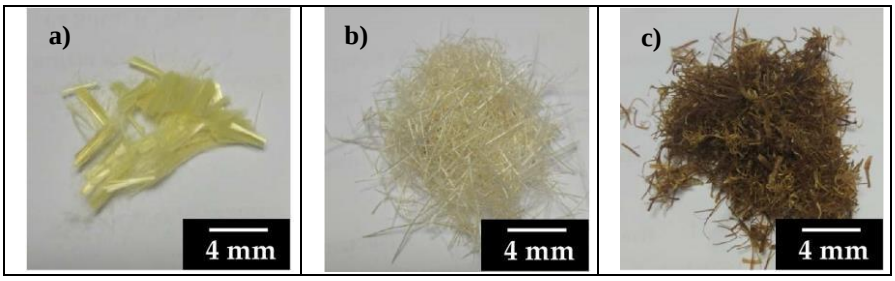

Figure 1. The visual aspect of the fibres: a) Aramid; b) Sisal; c) Biomass

The sisal fibres were used without any treatment. The biomass fibres, obtained from biomass material sourced locally in a pine tree forest, were treated following a patented process [53], where sodium hydroxide is the main chemical used.

The aramid and sisal fibres were purchased in roving spools of 100 m and an average length of 0.50 m, respectively. The biomass fibres were manually produced for this study, with an average length of 0.10 m. Knowing the influence that incorporated fibre size has on the performance of cement-based composites [57], and for them to be comparable, all fibres were manually cut with scissors to obtain the smallest length possible (≤ 5 mm). In Supplementary data, a histogram – Figure 3, based on 50 fibres from each fibre type, presented a normal distribution of the fibre length.

Due to these renders' use in multi-layered protective coating systems, a commercially available basecoat was also used [58], mainly formulated from Portland cement, resins, synthetic fibres and admixtures. This was the only layer of the multilayer coating system used since the objective was to evaluate the compatibility between the TRs (the insulation layer) and the basecoat mortar layer.

2.2. Preparation of the composites and samples

All the fibres were manually separated to avoid the formation of clumps, known for their negative influence on the composites' mechanical performance [59–61]. Prior to being mixed with the powder and the water, the fibres were conditioned at 20 ºC and 60%RH (relative humidity).

Four formulations were tested: *i)* aerogel-based render (TR reference); *ii)* aerogel-based render with aramid fibres (0.50% vol./vol. – TR aramid); *iii)* aerogel-based render with sisal fibres (0.10% vol./vol. – TR sisal); *iv)* and aerogel-based render with biomass fibres (0.10% vol./vol. – TR biomass). The selected percentages correspond to substitutions of powdered render quantities by volume. Those fibres volume fractions were selected based on the preliminary campaign presented in the *Supplementary material* (attached to the manuscript), where 0.10%; 0.25%; 0.50%; 1.00% and 2.00% fibre volumes were tested for all fibre types (Table 1 of supplementary data). The selection aimed to achieve higher compressive strength but assuring other properties like workability, consistency, bulk density at fresh and hardened states, no cracking during unmoulding, dynamic modulus of elasticity, compressive strength, flexural strength, and conductability tests (Table 4 in the Supplementary material). The

density of aramid fibres is higher than the density of other fibres and the render powder, thus higher compressive strength of the aramid fibre-enhanced render is expected, but no significant effect on the thermal conductivity.

For each formulation, three batches (around 1400 ml each) were produced, with the measurement of the fresh bulk density (in a 500 ml vessel) to control the variability of production. The kneading water quantities used a weighted ratio of water: render powder of 1.3:1.0, without considering the mass of the fibres, allowing to evaluate their influence on the render's workability and consistency.

Table 1 presents the mix ratios, by volume, their designation (where TR refers to Thermal Render, and where the percentage indicates the fibre volume, by total volume) and respective water content (by mass). With those amounts defined, the different components were weighted (render, fibres and water), then the kneading water was added to the mixing recipient and, after it, the render powder, where their mixture was carried out using a spatula. The fibres were then added in small amounts during the mixing process to ensure even distribution throughout the matrix. The moulds were previously coated with polyethylene film to improve their unmoulding and tamped down, to reduce the occurrence of trapped air. The lightweight concrete blocks are produced using lightweight expanded clay aggregates and cement-based binders and have the following characteristics: 500 × 250 × 200 mm^3 in size; made with lightweight concrete with a density of 1,200 kg/m^3. Then the render was directly applied over the blocks in two layers of 20 mm each, of the respective formulation. The basecoat was applied as indicated in the corresponding technical sheet [58], 28 days after the render's production.

Table 1. Composition, by total volume, of the mixes

Render formulation	**Reference render powder** [%]	**Reference render powder [m/m]**	**Aramid fibres** [%]	**Sisal fibres** [%]	**Biomass fibres** [%]	**Water: powder ratio** (by mass)*
TR reference (0.0%)	100.00	20% binders 37% aerogel	0	0	0	1.3
TR aramid (0.5%)	99.50		0.50	0	0	1.3
TR sisal (0.1%)	99.90		0	0.10	0	1.3
TR biomass (0.1%)	99.90		0	0	0.10	1.3

After production, the specimens were stored in a climatic chamber with a regulated temperature of 20 ± 2 ºC and RH of 65 ± 5% as referred to in the EN 1015-11 [62]. The specimens were then covered with a polyethylene bag

Caption: Fresh state: includes bulk density, consistency, workability, and air content; ρ – dry bulk density [kg m^{-3}]; E_d – dynamic modulus of elasticity [MPa]; f_t – flexural strength [MPa]; f_c – compressive strength [MPa]; Imp 3J – 3 Joule sphere impact diameter [mm]; Scl – PT pendulum hammer index; f_u – adhesion to the substrate and adhesion between render formulations and basecoat [MPa]; μ – water vapour diffusion resistance coefficient; C – capillary water absorption [kg m^{-2} $min^{-1/2}$]; A_w – capillary water absorption [kg m^{-2} $s^{-1/2}$]; DI – drying index; λ – thermal conductivity [W m^{-1} K^{-1}]; DVS – dynamic vapour sorption; SEM – scanning electron microscope; OM – optical magnifier; MIP – Mercury intrusion porosimetry; BET – N_2 adsorption-desorption isotherms at 77K; DRIFT – Infrared Fourier transform spectroscopy in diffuse reflectance mode; * - for the DVS fibres, silica aerogel, powdered render and render's paste were evaluated.

In Figure 2, different aspects of these initial stages can be observed. The test conditions, if not otherwise noted, were conducted under a temperature of 20 ºC and RH of 65%, with the samples in equilibrium with such conditions.

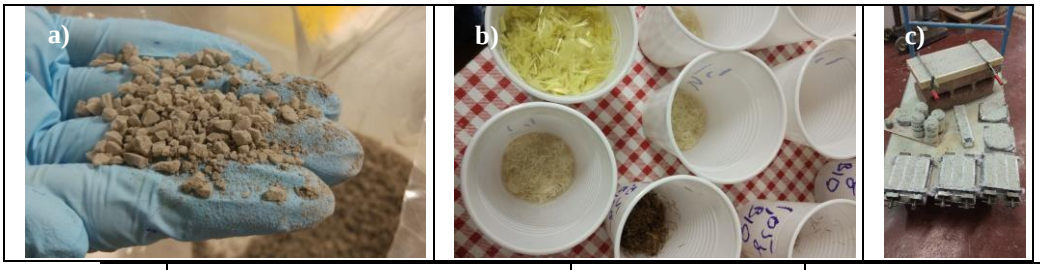

Specimens' shape	Fresh state	Mechanical								Physical				Microstructural			
		ρ	E_d	f_t	f_c	f_u	Imp 3J	Scl	$f_{u,}$	μ	C/A_w/ DI	λ	DVS	SEM/ OM	MIP	BET	DRIFT
Prismatic	3	6	6	6										3			
Prismatic halves					6					3	6	3			1	1	1
Cubic														1			
Cylinder I																	
Cylinder II																	
Lwt concrete block						5	5	5	4								
Small specimens													1*				

Figure 2. Preparation of the specimens. a) Aerogel-based thermal render; b) Fibres; c) Specimens aspect after production and application on the substrate

2.3. Experimental and analytical methods

2.3.1. Characterisation of the fibres

For the characterisation of the fibres, their length was evaluated after being manually cut. A set of 50 fibres, from each type, was observed using an optical microscope *Dino-Lite Edge 5Mpx Digital*, attached to a PC with image capturing and measuring software (*Dino-Lite image acquisition*). A histogram was then performed to evaluate the length distribution and compared to a normal distribution curve, where its results can be seen in the *Supplementary*

data. Their surface morphology was also observed using a Scanning Electron Microscope (SEM) *Hitachi S-2400 SEM*.

For the synthetic fibres, their diameter and density were considered, as stated in the data present in the respective technical datasheets. As for the natural fibres, due to their known variability [65–67], an evaluation was carried out (50 fibres from each type) using the same procedure and equipment as for their length study. The fibres were stretched when curled using colourless tape to bond the fibres against a paper, allowing them to remain stable for the measurement period.

For each one of the natural fibres, a histogram was created and compared to a normal distribution curve (see *Supplementary data.* The density of the natural fibres was determined according to the guidelines presented in the ASTM D 792 [68], using an analytical weighing scale with five decimal places, with ten fibres evaluated for each fibre type.

As natural fibres are known for their hydrophilic behaviour [69,70], retaining water, a simple test was adopted to evaluate possible influences on the workability and hydration reactions of the binders. Therefore, they were separately (by fibre type) placed inside a steel meshed bag for further testing.

For this test, 10 g of each fibre was used and placed inside individual steel meshed bags in an oven at 60 ± 5 ºC until their mass became constant (≤ 0.50% of the total mass, with two subsequent weightings, 24 h apart). After the fibres' mass was stable, they were immersed in a water container, and their mass was evaluated over time (Equation 1), where for each measurement the bags were placed onto a filter paper to eliminate excess water, only 237 evaluating the water entrapped in the fibres.

$$M_t = \frac{M_{wet} - M_{dry}}{M_{dry}} \times 100 \quad (1)$$

Where M_t is the mass at instant t [kg], M_{wet} is the fibres wet mass [kg], and M_{dry} is the fibres dry mass [kg].

2.3.2. Fresh state testing procedures

The testing procedures associated with the fresh state included bulk density, flow table consistency, workability and air content of the renders. The evaluation of the fresh bulk density was carried out in line with the EN 1015-6 [71]. The flow table consistency test followed the indications given in the EN 1015-3 [72]. The air content followed the indications of EN 1015-7 [73]. The workability was classified empirically, relative to the ease with which, by hand and using a spatula, the composite was mixed. For these tests, the EN 998-1 [21] only has requirements 245 associated with the values being declared.

2.3.3. Mechanical properties testing procedures

The bulk density, compressive and flexural strengths, visual crack observation during curing, and dynamic modulus of elasticity were assessed in the hardened state. Then the fibre-containing renders applied on lightweight concrete blocks were tested via adhesive strength (interface of the thermal render and the substrate), rigid body impact and pendulum hammer index. Moreover, the adhesive strength between the basecoat and the different TRs was also measured. All the tests were carried out at a minimum of 28 days after their renders' production.

The bulk density test during the hardened state followed the EN 1015-10 [74] guidelines for the geometric method, 253 using prismatic specimens (160 × 40 × 40 mm^3).

The dynamic modulus of elasticity was determined with a *GrindoSonic MK5 Industrial* equipment, evaluating this 255 property through the fundamental resonance frequency of the flexural and torsional vibration modes, according to the ASTM E1876-1 [75], using the same prismatic specimens as the bulk density, and compressive and flexural

strengths, since it is a non-destructive test.

The compressive and flexural strengths used the same previous prismatic specimens. Here, a Form+Test (model 505/200/10 DM1) equipment was used while following the standard EN 1015-11 [62]. However, to obtain the stress-strain curves and not only the peak (maximum) value, a *TML CDP 25* displacement transducer was also used, with a nominal capacity of 25 mm, and an *HBM datalogger Quantum MX840* universal measuring amplifier module, linked to a Personal Computer with the *Catman easy* software executed with a sampling rate of 20 Hz.

To evaluate if cracking occurred during the curing period, the specimens were visually inspected as they were being unmoulded to identify the presence of any cracks or distancing from the mould's boundaries.

Another tested aspect was related to the application of the different formulations over a lightweight concrete block.

The adhesion between the render formulations and the lightweight concrete blocks followed the guidelines present in EN 1015-12 [76], considering a render thickness of 0.04 m. Squared shape cuts (50 × 50 mm) were made from the render's surface to the block surface, using a grinder, and metal plates glued with epoxy. The adhesion test was conducted at a speed of 10 ± 1 mm min^{-1} on *Controls digital* equipment with a resolution of 0.001 kN and automatic recording of the peak value. As for the test scenario where a commercially available basecoat was applied over the surface of the renders, with a 0.003 m thickness, although following the same overall procedure, the cuts were only made into half of the renders' thickness, being at ≈ 0.02 m of the lightweight concrete block surface, allowing to evaluate the adhesive strength between basecoat and render. Since these renders are usually applied with protective multilayer coatings, due to their low mechanical resistance and high water absorption [39], it was evaluated if the fibres influenced the adhesion between render and basecoat.

Finally, the superficial impact resistance of the renders was assessed using the rigid body impact (LNEC FE Pa 25 procedures [77,78]) using a *Martinet-Baronnie* with a metal sphere, where five test points were chosen for an equivalent impact of 3J, observing: *i)* the diameter of the impacts [mm]; *ii)* and the presence of microcracks, or cracks, at the impact area. The pendulum hammer hardness index was evaluated using a *Proceq pendulum sclerometer type PT nr 6299*, following the RILEM MS D.7 [79] for five points. Both tests allowed to evaluate the influence of the fibres on the superficial shock resistance of different renders.

Considering the requirements of the EN 998-1 [21], the bulk density only demands the declaration of a range of values. Regarding the compressive strength, the minimum value, class CS I, is 0.40 MPa. For the adhesion, the

performance of the material must be greater than or equal to the declared value, as well as the need to indicate the type of rupture. The remaining tests do not present any requisites.

2.3.4. Physical testing procedures

The physical characterisation of these formulations covered evaluating the thermal conductivity at the dry-state at 10 ºC, the capillary water absorption, the drying index, the water vapour permeability, and, finally, the Dynamic 289 Vapour Sorption (DVS) of the individual materials - powdered render, silica aerogel, fibres, and paste.

The thermal conductivity evaluation followed the specifications of the EN 1745 [80], as indicated in EN 998-1

et al. [81,82], referring to the transient linear probe method, using *Applied Precision*. The measurements are in accordance with ASTM-D-5334 [83], [84] and EN 22007-2 [85]. All tests were performed with a mean reference temperature of 20 ± 3 by using the method of ISO 10456 [86], considering the II a) conditions - ing a temperature conversion coefficient of 0.003 K^{-1}. The linear probe used has a measurement range between 0.015 and 0.050 W m^{-1} K^{-1}, an accuracy of 5 % of the reading value + 0.001 W m^{-1} $^{-1}$ K^{-1} [87] were used with ≥ 65 mm in diameter and ≥ 130 mm in height, filled with the renders and previously pre- fresh state. After 28 days, the specimens were placed in an oven at 60 °C until 300 their mass stabilised (± 0.10%), for at least three days. They were immediately wrapped in plastic shrink to room temperature before being tested. . Following the EN ISO 1015-18 [88], the half samples resulting from the flexural strength tests were re-used in the capillary test.

However, the applied calculation methods were both the ones presented in the EN ISO 15148 [89] (A_w) and in the EN ISO 1015-18 [88] (C), allowing a more thorough evaluation of the formulations' performance. The sides of the 306 samples were coated with paraffin wax to obtain a directional flux of water in the capillary test. Then, the bottom 307 faces were immersed in a water depth of 5 ± 2 mm and weighed at 5, 10, 20, and 30 min, and then at 1, 1.5, 2, 4, 308 8, 12 and 24 hours, being their mass continually assessed until stabilisation.

The drying kinetic evaluation was based on the EN 16322 [90] and was carried out after full water saturation of the samples used in the capillary water absorption test. It was considered that the saturation was achieved when

the difference between two consecutive weightings, at an interval of 24 hours, was less than 0.10% of the previous mass of the specimen. The test starts by evaluating the saturated mass of all the specimens. Then, to evaluate the drying properties, the specimens are placed upside-down, and it is annotated for the hour in which the test started. The specimens were then maintained in a controlled environment with 23 ºC of temperature and 53%RH during the testing period. The test was carried out with several consecutive measurements, always annotating the time and the specimens' mass. When the specimens showed a weight variability below 0.10% for three consecutive evaluations, separated at least 24 h, the test ended, being possible to obtain their final mass. From there, the residual amount of water of each specimen, per unit area, could be calculated. With these measurements, it is possible to evaluate the drying rate of the first drying phase (D1), more linked to the transport of water to the surface followed by evaporation, and also the second drying phase (D2), which is characterised by a decrease in liquid water transport, increasing the water vapour diffusion. With both regression curves, it is possible to mathematically calculate the intersections between them, obtaining the knick-point (t_k in [h]), which is the time of the transition between those two phases. To improve this evaluation, it was also calculated the drying index (DI), which represents the material resistance to water evaporation. This was calculated using the *Matlab* software since it results from the area quantification below the obtained curve.

The water vapour permeability quantifies the water vapour transfer through the tested materials, under a vapour pressure gradient, once a steady state is reached. This property directly influences the water vapour's circulation resistance in construction materials, potentiating their drying for higher water vapour permeability. Although for renders, the EN 1015-19 [91] is used, the EN ISO 12572 [92] allows the same parameters to be characterised with more detailed guidelines, while both are comparable. Therefore, in this study, the latter reference standard was followed. This evaluation used the dry cup test method ($\varphi \approx 0$%RH). Each mixture used three cylindrical samples, with an average area of 0.02 m^2. These samples were conditioned following the EN ISO 12572 [92], and after reaching stabilisation, each sample was placed over a plastic cup, which had a 0.015 m layer of the chosen desiccant inside (silica gel aggregates with diameters between 1 and 3 mm) which had been previously dried in an oven at 100 ºC. Then, the render samples closed the top of the cup, presenting an estimated air layer of 0.01 m between them and the silica gel. The side area between the render's sample and the plastic cup was then sealed with a hydrophobic and vapour-impermeable material and a mixture of paraffin wax and microcrystalline wax to ensure that the vapour flux was only through the sample's exposed surface. The test cups were then maintained in a chamber with controlled conditions (23 ± 0.5 ºC and 50 ± 3%RH) and regularly weighted, while also annotating

the barometric pressure, air temperature, and RH in each measurement. Due to the vapour pressure gradient, a vapour flux could be originated through the sample's surfaces allowing the silica gel to absorb the moisture and increase its mass over time, allowing to determine the water vapour permeability.

To explore the individual water vapour sorption and desorption properties of the render powder, aerogel, fibres, and paste, their characterisation was carried out using a DVS [93,94] *Intrinsic analyser* from *Surface Measurement Systems*, equipped with a microbalance. The samples, with a mass under 1 g, were dried until the mass stabilised. Then, for a stable temperature of 25 ºC, RH of the chamber was increased in 5%RH steps, from 0 to 95%RH during the time needed for the sample's mass to stabilise in each step (sorption). After reaching the maximum RH value, it was reduced in steps of 5%RH (desorption) until arriving at 0%RH, allowing to evaluate the existence of any hysteresis.

Concerning the EN 998-1 [21], class T1, for TRs, is established as the most demanding, with maximum thermal conductivity, at 10 °C and in the dry state, of 0.100 W m^{-1} K^{-1}. The same standard defines that, for TRs, the water vapour permeability coefficient (μ) must be ≤ 15, and the capillary water absorption must present a value below 0.40 kg m^{-2} $min^{-0.5}$ (W1). The remaining tests do not present any requirements on this standard.

2.3.5. Microstructural analysis

For the microstructural characterisation, which allows a better understanding of the materials' behaviour, an optical magnifier (OM), a SEM, a mercury intrusion porosimeter (MIP), and the N_2 adsorption-desorption isotherms at 77 K (BET) were used. For molecular characterisation, the infrared Fourier transform spectroscopy in diffuse reflectance mode (DRIFT) was employed.

The use of a *Dino-Lite Edge 5Mpx Digital* OM allowed observing both the integrity of the aerogel granules and their distribution within the paste. It also allowed verification of the fibre's distribution and orientation inside the matrix, while also evaluating their possible influence on the scattering and integrity of the aerogel granules. Here it was observed that the broken halves resulted from the flexural strength tests.

To further analyse the microstructure and morphology of these formulations, namely the areas of most significant interest associated with the interface aerogel/paste, fibres/paste/aerogel, and the fibres surface, distribution, connection and influence on the render's microstructure, a SEM *Hitachi S-2400*, operated at 20 kV was used. A palladium film was sputtered on the surface of the samples to prevent surface change. With this microstructural

analysis technique, it is possible to evaluate the samples' conditions, the existence of pores, constituent degradation, and hydration products from chemical reactions between binders and water [95,96].

The IUPACs pore diameter range classification was followed [97]: micropore (internal diameter < 2×10^{-3} μm), mesopore (internal diameter between 2×10^{-3} and 5×10^{-2} μm) and macropore (internal diameter > 5×10^{-2} μm).

For further analysis of the renders, a MIP *AutoPore IV 9500* from *Micromeritics*, with a maximum intrusion volume for low and high pressure of 1×10^{5} mL g^{-1} was used. This equipment provides pressure versus intrusion data, generating volume and size distributions using the Washburn equation [98,99]. As widely known, the pore structure is crucial in understanding the formation, structure, and potential use of materials, influencing their properties and, consequently, their behaviour. Water absorption, water vapour permeability, density and even other factors like mechanical strength, are influenced by the pore structure [18,100], with capillary pores (considered meso to macropores in IUPACs classification, which range from 2×10^{-3} to 1×10^{1} μm – influencing the strength and water vapour and liquid behaviour [101]) and air voids (above the range of capillary pores mainly influencing strength [101,102]) being the ones with the highest influence on cement-based materials according to Aligizaki [101] and Mindess et al. [102].

Two more aspects were also evaluated based on the MIP results: the threshold pore diameter and the critical pore diameter. The threshold pore diameter is defined as the intersection between two tangents of the cumulative curve, calculated as described by Berodier *et al.* [103], specific to each of the analysed materials. In qualitative terms, it is the largest pore diameter at which significant intruded pore volume is detected. According to Winslow and Diamond [104] and Mindess *et al.* [102], this diameter corresponds approximately to the minimum diameter of channels that are continuous throughout the sample, forming a continuous network, marking the onset of percolation, since it is the widest, most accessible, a path for fluid transport in the cement-based materials [105]. Finally, the critical pore diameter corresponds to the pore size, where the steepest slope of the cumulative porosity curve is found [103]. This point is the pore diameter through which mercury penetrates the bulk of the specimen, *i.e.* it is the most frequently occurring pore diameter in interconnected pores that allows maximum percolation [104]. The critical pore size controls the material's transmissivity and is usually preferred over the threshold pore diameter since it is found more easily and accurately [101].

In the BET technique, which mainly focuses on the micro to mesopore classification according to IUPACs classification, the specific surface area and pore size distribution were estimated by analysing N_2 adsorption

isotherms at 77K, obtained with a *Micromeritics ASAP 2020*. The samples were degassed by heating under a vacuum to remove any adsorbed impurities, gases, or vapours. For their evaluation, the average size distribution of mesopores was estimated by the BJH (Barret-Joyner-Halenda) model applied to the adsorption branch [97]. Nonetheless, care must be taken to correctly use this technique because the BET equation is only valid if the C parameter value is between 5 and 150 [97]. If the C value exceeds 150 or appears negative, there is no possibility of applying the BET model because the material is not mesoporous [97].

The last technique used for this type of analysis is related to the evaluation of the molecular structure of the render, using the Fourier Transform Infrared Spectroscopy (FTIR) technique used in diffuse reflectance (DRIFT) mode on a *Mattson RS1* spectrometer with a *Specac* selector and a broadband *MCT detector* (4,000 to 400 cm^{-1}). The spectra were plotted at a 4 cm^{-1} resolution, resulting from ratioing 500 added scans per sample against the same number for the background (ground KBr). To analyse the obtained spectra, which are based on the fact that each chemical specie has characteristic vibrational modes, giving several spikes that are then compared with other known spectra [106–110] and identified. This technique is used to identify existent chemical species and possible chemical reactions between the components of the render.

3. Results and discussion

3.1. Fibres characterisation

The supplementary data presents the fibres' length and diameter (sisal and biomass) distribution. The mean length of the fibres was $4.41 \times 10^3 \pm 2.42 \times 10^3$ μm (or 4.41 mm). This is related to the fact that they were manually cut, introducing some significant variability. When considering the diameter, the synthetic fibres presented mean values around 2.0×10^1 μm, within their technical data sheets and supported by the SEM images (Figure 3) and more homogeneous than the ones of natural origin, Table 4.

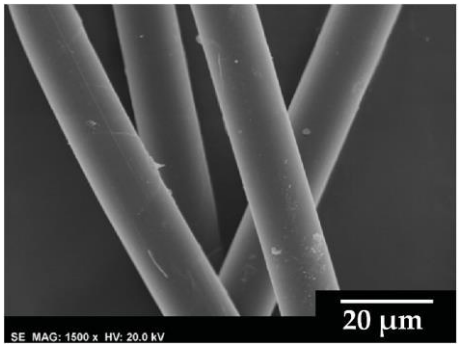

Figure 3. Aramid fibres viewed on a SEM

Table 4. Properties of the fibres - experimentally obtained

Fibre types	Average length [µm]	Average diameter [µm]	Aspect ratio	Water absorption at 48 h [% mass]	Density [kg m^{-3}]
Aramid	$4.41 \times 10^3 \pm 2.42 \times 10^3$	15	294	3.1	1440*
Sisal		209	21	178.5	767
Biomass		253	17	340.0	731

Note: * - Values present in technical datasheets/literature [56,115,116]

When observing the fibres' morphology, different magnifications had to be used due to their varied diameters. This analysis shows that the synthetic fibre (Figure 3) presented smoother surfaces contrasting with the natural organic fibres (Figure 4), which have a rough surface. It was also possible to verify that the biomass fibres were not completely individualised and still had some extractives, since each fibre seemed to present a diameter of 8.0 µm (Figure 4 b)) – seen in the magnification inside the blue box. However, due to the manual process involved in their obtention, they could not be further individualised.

Regarding water absorption, the results are presented in Figure 5. The natural fibres present a much higher water absorption than the synthetic fibres due to their highly hydrophilic nature [65]. This can negatively impact cement hydration [117] and factors such as microcracking of the matrix (fibre swelling) and the interface paste/fibre. However, this effect can be minimised in smaller sizes and contribute to the matrix densification while improving its mechanical properties [12].

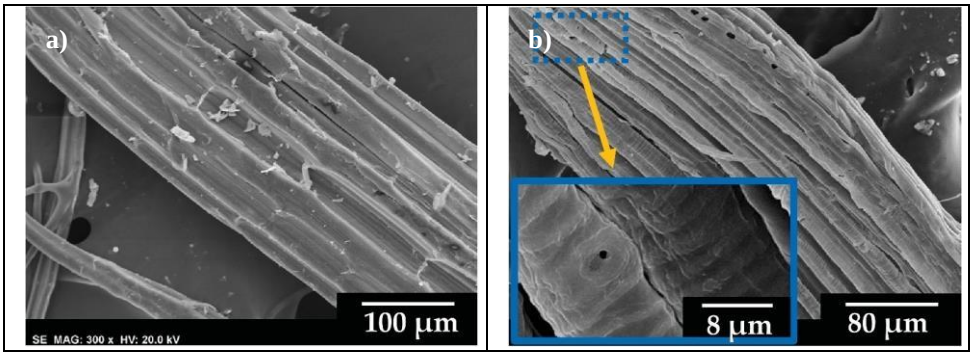

Figure 4. SEM images of the sisal fibres (a)) and biomass fibres (b)). The blue box in b) shows a more detailed view of the biomass single fibre diameter

As observed in Table 4, the aramid fibres showed insignificant water absorption, being in line with the results presented in their technical datasheets [56]. For the sisal, although presenting values higher than those reported by Arséne *et al.* [65], they seem to be similar to other researchers' results [118,119], which might be related to the high variability associated with natural fibres. As for the biomass fibres, due to their novelty, there are no known references. However, when compared to Eucalyptus or Banana fibres (643% and 407% of mass increase over the dry fibres, respectively) [120,121], they present lower water absorption.

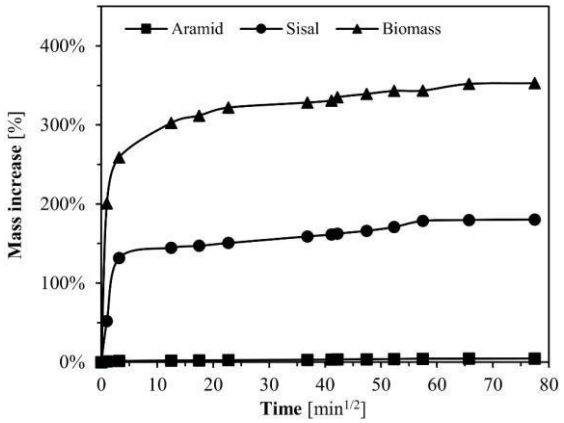

Figure 5. Water absorption of the fibres in relation to their initial dry mass

3.2. Fresh state characterisation

The characterisation of the fresh state properties for all the tested formulations is presented in Table 5. Due to the fibres' diameter and their amounts, the mixes presented different numbers of fibres per dm^{-3}, with aramid, due to their lower diameter, having a higher value than the natural fibres, also related to the higher volume of insertion (0.5% *vs* 0.1% (vol./vol.)). While keeping the same water to powder ratio, the workability could be maintained above or equal to 'good', directly related to the consistency values.

Table 5. Mixes and fresh state properties

Render designation	Fibres [dm^{-3}]	Water: powder ratio	Cons [mm]	Workability	[kg m$\rho_{fresh}$$^{-3}$] Air content[%]
TR reference (0.0%)	0.00 × 10^{0}	1.30	143.5 ± 1.5	293 ± 3	21.5 ± 0.5
TR aramid (0.5%)	6.58 × 10^{6}	1.30	121.1 ± 2.3	Excellent	
TR sisal (0.1%)	6.81 × 10^{3}	1.30	139.7 ± 3.5	Good	310 ± 4	19.5 ± 1.0
TR biomass (0.1%)	4.61 × 10^{3}	1.30	139.1 ± 3.8	Excellent	297 ± 5	22.0 ± 1.0
				Excellent	299 ± 5	22.5 ± 0.5

Note: ± SD – standard deviation. **Parameters:** Cons – consistency [mm]; ρ_{fresh} – bulk density fresh state [kg m^{-3}].

With the use of the natural fibres, a slightly higher fresh state bulk density (≈ + 2%) was obtained, even when the

mixtures containing natural fibres presented slightly higher air content (more 0.5 to 1%). This can be related to the

fibres' higher density (higher than the paste) influencing the render's bulk density. Usually, in cement-based

composites, this is the opposite, since the fibres present lower values than the matrix. When considering the render formulation containing aramid fibres, a lower air content (by 2%) and higher bulk density (by 5%) was reached, attributed to a more compact mixture, where the workability was only classified as 'good'.

3.3. Mechanical characterisation

The results for the mechanical characterisation of the formulations are presented in Table 6.

Table 6. Mechanical characterisation of the formulations

Render designation	ρ_{hard} [kg m^{-3}]	$f_{c,peak}$ [MPa]	$f_{t,peak}$ [MPa]	Cracks during curing?	E_d [MPa]
TR reference (0.0%)	159 ± 3	0.185 ± 0.002	0.092 ± 0.003	No	51.3 ± 2.3
TR aramid (0.5%)	165 ± 4	0.208 ± 0.004	0.165 ± 0.012	No	77.4 ± 4.6
TR sisal (0.1%)	160 ± 3	0.193 ± 0.002	0.093 ± 0.002	No	49.2 ± 2.0
TR biomass (0.1%)	162 ± 2	0.190 ± 0.003	0.092 ± 0.002	No	48.3 ± 1.9

Note: ± SD – standard deviation. **Parameters:** ρ_{hard} – bulk density hardened-state [kg m^{-3}]; $f_{c,peak}$ – compressive strength peak value [MPa]; $f_{t,peak}$ – flexural strength peak value [MPa]; E_d – dynamic modulus of elasticity [MPa].

The bulk density results remain very similar to the reference (TR reference), with an average value of 160 kg m .

-
3

The aramid-containing formulation (TR aramid) presented a higher value (≈ + 4%), which can be related to a 467 higher fibre quantity and density.

As for the compressive and flexural strengths, it can be seen in Table 6 that the fibres' insertion led to an average

increase of both properties, whereas in Figure 6, it is possible to visualise the respective stress-strain curves. When

analysing their performance, there was an increment of the compressive strength (3-12%) when fibres were added,

with aramid (0.50% vol.) showing the highest increase. The flexural strength, although also increased, was almost

negligible for the natural fibres (with lower density), but for the aramid fibres, it increased by ≈ 80%. The density and orientation of the fibres could justify the differences in both strengths. Although the 0.5% (vol.) of aramid

fibres improved the mechanical performances when compared to the reference, these values are half of those

referred by the EN 998-1 [21], not fulfilling the minimum requirement for external coating mortar application (0.40 MPa); however, similar aerogel-based TRs, already developed, also present low values, some of them below 0.15 MPa [30,122,123], and are being applied in a multilayer system. These results highlight the importance of evaluating the suitability of EN998 requirements for super-insulating materials.

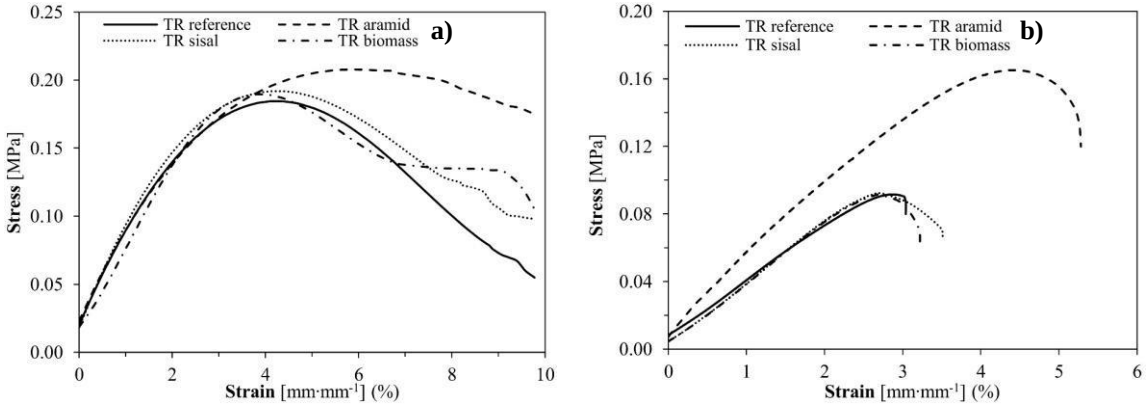

Figure 6. Stress-strain curves: a) compressive strength; b) flexural strength

Figure 6 a) shows that all renders present an ability to deform 3 to4%. It can also be seen that TR biomass showed an initial higher deformation, probably related to the higher degree of debris that these fibres have on their surface, due to the isolation process, or even to a weaker connection to the matrix, allowing some s lippage. All fibre-containing formulations showed a higher capability to deform while holding some stress after their peak compressive strength was surpassed (above a 4 to 5% strain). As for the TR aramid formulation, its highest compressive strength value was at ≈ 5% strain, but even after that point, it continued to maintain a compressive strength higher than TR reference, until a 10% strain, which was limited by contact with the test equipment.

Figure 6 b) shows that the highest influence of the natural fibres' insertion on flexural strength was not in terms of

the maximum flexural strength, but by enabling their specimens to deform longer while handling some stress. Here, the aramid fibres showed a significant increase in the flexural strength, not only in its maximum value but also in the ability to, while deforming, still handle stress. The orientation of the fibres and the presence of resin in the matrix could justify this behaviour.

Here, once again, the biomass fibres' performance suggests that since their surface presents extractives and impurities - see corresponding SEM images -, it did not allow an adequate fibre bonding with the matrix, also associated with a higher water affinity, influencing their performance due to slippage inside the matrix.

Upon visual inspection during the curing period, no cracks on the renders' surface or between the moulds and the renders were observed. This could be initially expected due to the high-water quantity used for the mixing.

For the dynamic modulus of elasticity, as expected after visualising the stress-strain curves, the TR aramid showeda higher value than TR reference. The natural fibres maintained a similar performance to the reference since theyshowed values within their standard deviation. However, these values are still below current TR formulations, withthe TR aramid formulation showing a higher degree of similarity (commercial TRs usually present values above100 MPa [124]). These lower values are an indicator of deformability capabilities, moving with the substrate while 502 not cracking [125], which can also contribute to the lack of cracks in the moulds' perimeter.When developing render formulations for buildings' applications, a key factor is their behaviour when applied toa substrate (*e.g.* lightweight concrete block). Table 7 presents the results of the adhesive strength between therenders and substrate and between the renders and basecoat, as well as the results for the 3 J impact tests, where 506 the diameter of the impact and the existence of cracks for each one of the five impacts were assessed.Figure 7 shows some aspects of the tests with and without the applied basecoat. The only difference between thetests was verified on the TR aramid formulation, in which, after the detachment, the specimen remained connectedto the block render through the fibres, but without further increasing the adhesive strength value. The fibres' introduction only resulted in adhesive strength improvements for TR aramid (≈ + 13%), whereas the natural fibres' formulations maintained a similar performance to TR reference. All formulations presented cohesive rupture in the render (B), indicating good adhesion to the substrate. The increase in adhesion of TR aramid could be related 513 to the better internal cohesion of the render (interconnection between fibres and aerogel).

Table 7. Synthesis of the adhesion and impact test results

Render designation	f_u [MPa]	$f_{u,basecoat}$ [MPa]	Imp 3 J ϕ [mm]	**Cracks after impact?**	**Scl index** [-]
TR reference (0.0%)	0.066 ± 0.003*	0.065 ± 0.004*	31.5 ± 1.5	3/5	59.3 ± 2.7
TR aramid (0.5%)	0.075 ± 0.004*	0.073 ± 0.003*	29.9 ± 1.0	0/5	62.4 ± 1.8
TR sisal (0.1%)	0.067 ± 0.002*	0.065 ± 0.003*	31.0 ± 1.8	1/5	59.5 ± 1.9
TR biomass (0.1%)	0.066 ± 0.003*	0.066 ± 0.004*	31.2 ± 1.6	2/5	59.4 ± 1.7

Note: ± SD – standard deviation; * - All tests presented a 'B' fracture pattern: cohesive in the aerogel-based render.
Parameters: f_u – adhesion [MPa]; $f_{u,basecoat}$ – adhesion between render and basecoat [MPa]; Imp 3 J ϕ – 3 Joule sphere impact 517 diameter [mm]; Cracks – number of impacts with cracks in a total of five; Scl – pendulum hammer hardness index [-].

When considering the renders' surface coating with the basecoat, Figure 7 d), showed that those materials presented

good adhesion since the fracture was kept cohesive in the render. The basecoat remained strongly connected to the

aerogel-based fibre-enhanced renders.

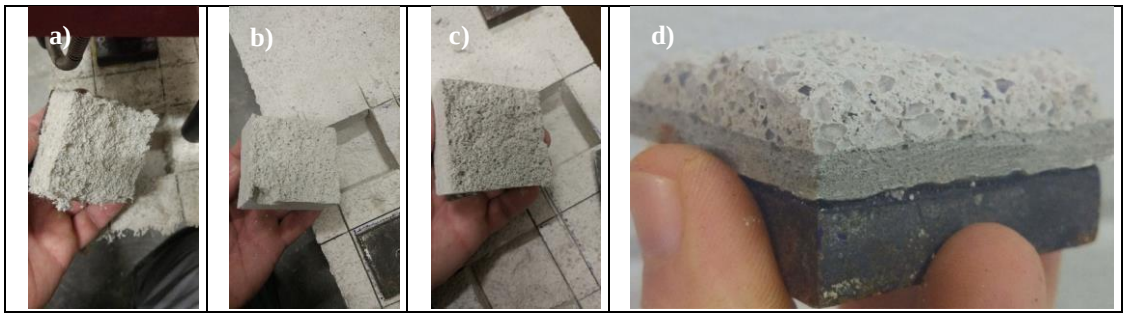

Figure 7. Adhesion tests: a) TR aramid; b) TR sisal; c) TR biomass; d) TR sisal and basecoat

While evaluating the 3 J impact resistance diameters (Figure 8) a similar trend to the adhesive strength was seen.

The TR aramid formulation showed a decrease of ≈ 5% in the impact diameter, while the natural fibre formulations

the metal sphere's impact area showed similar to slightly better performance than the TR reference. In terms of visible cracks, the TR aramid showed no cracks in all test points, where TR sisal and TR biomass slightly improved this aspect over the TR reference. When cracks were identified (red arrows in Figure 8), they presented a similar scattered pattern around

The pendulum hammer index showed a higher value for the TR aramid than for the TR reference (≈ + 5%), with the other formulations being similar to the TR reference.

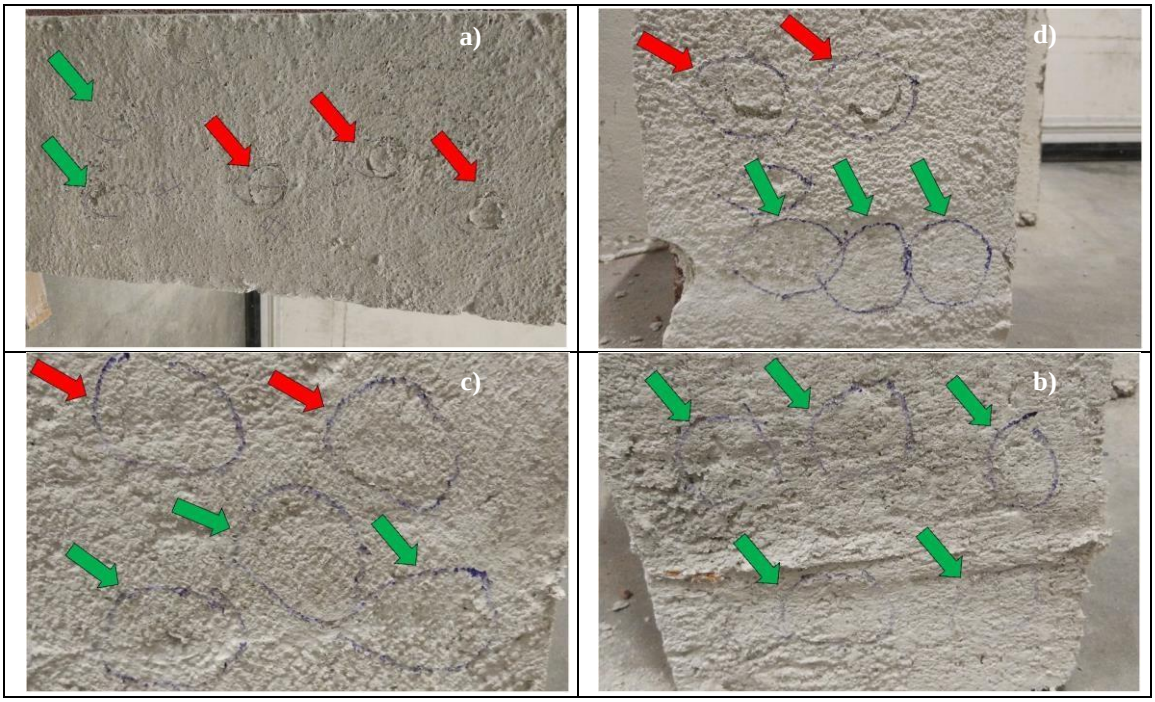

.

Figure 8. Formulations after the 3 J impacts: a) TR reference; b) TR aramid; c) TR sisal; d) TR biomass - green arrows = no cracks and red arrows = cracks

3.4. Physical characterisation

Table 8 presents the dry-state thermal conductivity (λ), at 10 ºC, obtained for the different formulations. It can be seen that these renders present very low thermal conductivity, being lower than other materials classified as classic thermal insulators (*e.g.* EPS λ ≈ 0.036 W m^{-1} K^{-1} [126]). However, the fibre's incorporation led to a thermal conductivity increase, but with low significance, since the results were within the standard deviation values. 537 Nonetheless, this can be related to the higher thermal conductivity of the fibres when compared with silica aerogel (λ ≈ 0.012 W m^{-1} K^{-1} [127]), since cellulosic fibres present a λ ≈ 0.050 W m^{-1} K^{-1} [12] and aramid fibres a λ ≈ 539 0.040 W m^{-1} K^{-1} [116].

Table 8. Thermal conductivity in the dry-state and at 10 ºC

Render designation	$\lambda_{10ºC,dry}$ [W m^{-1} K^{-1}]
TR reference (0.0%)	0.0293 ± 0.0031
TR aramid (0.5%)	0.0315 ± 0.0019
TR sisal (0.1%)	0.0298 ± 0.0027
TR biomass (0.1%)	0.0306 ± 0.0032

Note: ± SD – standard deviation; **Parameters:** $\lambda_{10ºC,dry}$ – thermal conductivity at 10 ºC in the dry-state.

The results for the capillary water absorption are shown in Table 9. The incorporation of fibres led to lower water absorption coefficients (≈ less 70%) but also impacted the capillary progression of the water absorption (Figure 9 544 with the standard deviation marked for each point): type 'A' curve for TR reference *vs* type 'B' curves for the other 545 formulations.

Table 9. Results of the water absorption coefficients

Render designation	**Water on top?**	**$A_{w,24h}$** [kg m^{-2} $s^{-1/2}$] – **Curve type**	C [kg m^{-2} $min^{-1/2}$]
TR reference (0.0%)	Yes @ 8 h	$1.09 \times 10^{-1} \pm 1.31 \times 10^{-3}$ - A	$9.00 \times 10^{-1} \pm 4.01 \times 10^{-2}$
TR aramid (0.5%)	No	$2.86 \times 10^{-2} \pm 1.01 \times 10^{-3}$ - B	$3.40 \times 10^{-1} \pm 2.10 \times 10^{-2}$
TR sisal (0.1%)	No	$3.25 \times 10^{-2} \pm 1.12 \times 10^{-3}$ - B	$4.00 \times 10^{-1} \pm 3.23 \times 10^{-2}$
TR biomass (0.1%)	No	$3.10 \times 10^{-2} \pm 1.30 \times 10^{-3}$ - B	$3.53 \times 10^{-1} \pm 3.37 \times 10^{-2}$

Note: ± SD – standard deviation; **Parameters:** $A_{w,24h}$ – capillary water absorption according to the EN ISO 15148 [89] [kg m^{-2} $s^{-1/2}$]; Curve type – classification according to the curve shape as indicated in the EN ISO 15148 [89]; C – capillary water absorption according to the EN ISO 1015-18 [88] [kg m^{-2} $min^{-1/2}$].

With these results, it can be reasonably inferred that the TR reference shows a stronger capillary network with higher connectivity due to the quick water progression through the material, which after only 8 hours it was already seen water on the top of the samples. After an initial stage where the material was dry and, capillary transport was

fast, the samples with fibres quickly changed to a stage where the water progression slowed. Here the fibres seemed

554 to obstruct capillaries and, due to the presence of air pockets inside the matrix (natural fibres), hindered the capillary water progress [128]. The reference started to stabilise after ≈ 12 hours, whereas the other formulations

only showed similar signs after ≈ 90 hours.

With such behaviour, there was a reduction in the initial suction, where the use of fibres in the formulation seems to influence the TR, acting as an initial water absorption barrier, and delaying the process. When the performance of different fibre-containing formulations is compared, it is seen that the formulation with aramid (TR aramid) showed a lower water absorption, with this behaviour being expected as aramid showed less affinity to water than the natural fibres. Compared with other TRs (A_w of 2.96×10^{-2} kg m^{-2} s$^{-1/2}$ [18]), the incorporation of fibres enabled a similar performance, since, without their inclusion, the water absorption coefficient was higher.

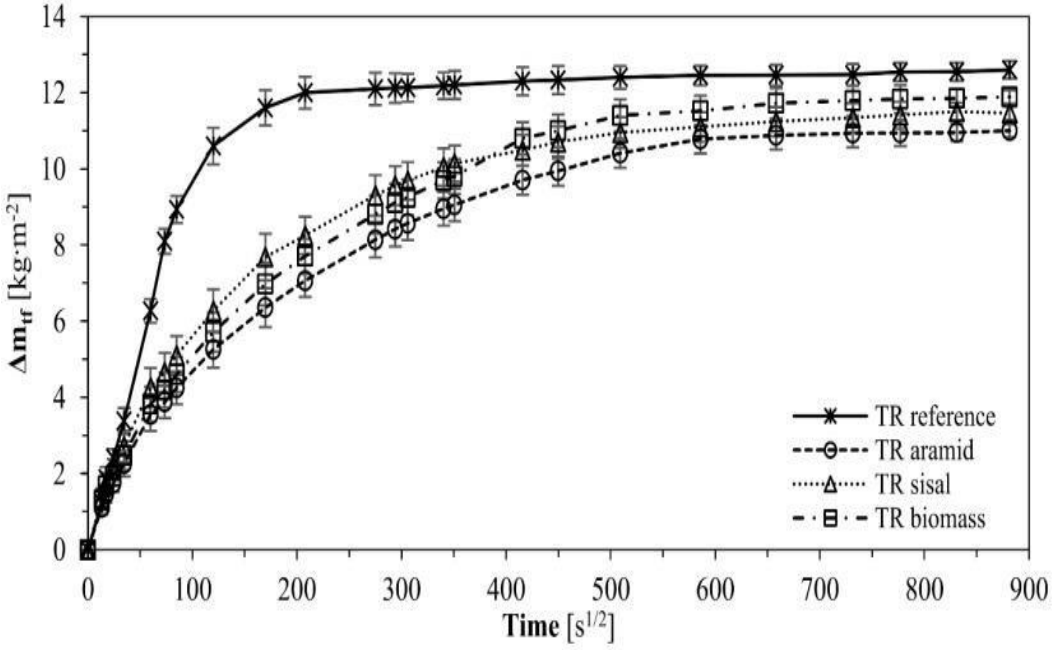

Figure 9. Water absorption as a function of the square root of time - an indication of the standard deviation per measurement

In Table 10 and Figure 10, the results for the drying properties of the formulations can be seen. Here, as a reference, the drying kinetic with the optimum performance is obtained when the D1 and D2 phase rates are the highest, while DI is the lowest since it is a parameter that relates to the drying resistance.

Table 10. Synthesis of the adhesion and impact test results

Render designation	D1 phase [kg m^{-2} h^{-1}]	D2 phase [kg m^{-2} h$^{-1/2}$]	t_k [h]	DI
TR reference (0.0%)	0.172 ± 0.011	1.483 ± 0.021	23.1 ± 1.1	0.20 ± 0.01
TR aramid (0.5%)	0.157 ± 0.012	1.485 ± 0.020	34.8 ± 0.9	0.19 ± 0.01
TR sisal (0.1%)	0.159 ± 0.015	1.514 ± 0.025	33.5 ± 0.8	0.18 ± 0.01
TR biomass (0.1%)	0.162 ± 0.014	1.522 ± 0.022	32.6 ± 0.9	0.18 ± 0.01

Note: ± SD – standard deviation; Parameters: t_k – knick point [h]; DI – drying index.

As expected, the fibre-containing formulations showed less absorbed water at the beginning of the test. This, as previously discussed, seems related to some capillary interference of the fibres. As for the total duration of the test, both natural fibres took more than 24 hours to stabilise compared to the reference and the aramid formulations. This, as in the DVS results for water vapour uptake by the fibres, also showed increased water affinity of the natural fibres.

The D1 phase associated with the transport of liquid water to the surface, followed by evaporation, can be attributed to larger pores (capillary range), and the good interconnectivity of the renders' pore channels [129]. It was then seen that the reference showed a higher rate since it also showed a higher capillary absorption. The D1 results (Figure 10 a)) seem related to the results obtained during the capillary water absorption test. For the D2 phase, Figure 10 b), the natural fibre formulations presented a higher rate. In this phase, there is an association between the reduction of liquid water transport and a progressive increase in water vapour diffusion [95], which contrary to the liquid water transport, also occurs in the small capillary pores' range, influencing the gas permeability [130]. Knowing this fact, these formulations are likely to show higher water vapour permeability results.

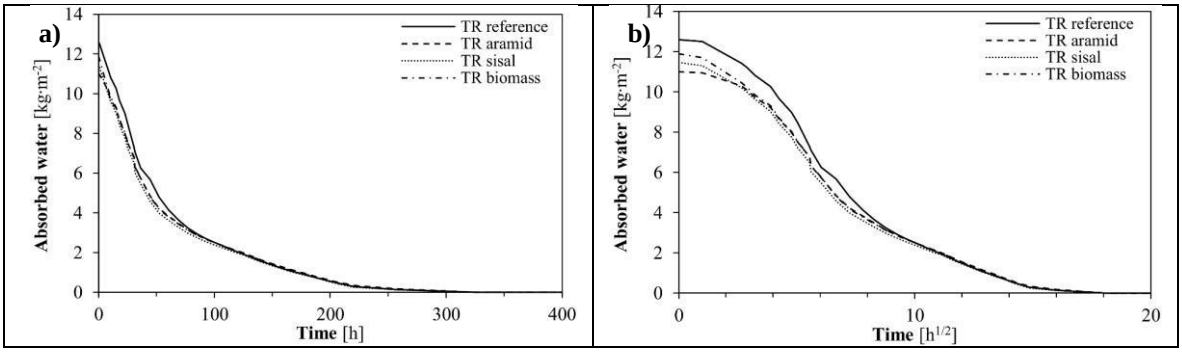

Figure 10. Drying curves: a) D1 phase; b) D2 phase

As the reference showed a stronger capillary grid than the fibre -containing formulations, translated by the higher capillary water absorption, the transition (knick-point, t_k) was sooner since the water in the capillaries was readily available for surface evaporation [131]. Finally, the DI showed similarities between the formulations, with the natural fibre-containing formulations showing a very slight decrease.

The use of fibres in renders is usually associated with a significant increase in the DI due to their higher water affinity [132,133]. However, this was not the case since it remained similar when considering the respective standard deviations associated with the samples. This can be related to the small number of introduced fibres and the potential microstructural impact their use had over the reference formulation [95], not significantly influencing this drying phase. In terms of overall performance, they showed higher DI values than other renders (DI ≈ 0.15 for test times under 80 hours [134]), indicating a higher drying resistance, even with the test times being different.

This test should be considered as an indicator of the drying potential of the formulations, since their ability to dry whilst in-service is a function of several factors (*e.g.* surface covering, solar radiation, temperature), in which the non-uniformity of rain and wetting of the thermal insulation materials, immediately followed by drying conditions, also plays a significant part.

The water vapour permeability results are presented in Table 11, where Figure 11 shows the average kinetic mass during the test. For all the formulations, the steady-state was reached after six days. The test continued until more than five measurements, within the required variability, could be obtained. Then it was possible to obtain the water vapour flow rate (G), enabling to obtain the water vapour diffusion resistance factor (μ) and the water vapour diffusion-equivalent air layer thickness (s_d).

Table 11. Synthesis of the water vapour permeability results

Render designation	G [kg s^{-1}]	δ [kg m^{-1} s^{-1} Pa^{-1}]	μ [-]	s_d [m]
TR reference (0.0%)	2.013×10^{-8}	1.400×10^{-11}	13.7 ± 0.5	0.27 ± 0.01
TR aramid (0.5%)	2.082×10^{-8}	1.449×10^{-11}	13.3 ± 0.9	0.27 ± 0.03
TR sisal (0.1%)	2.068×10^{-8}	1.518×10^{-11}	12.7 ± 0.4	0.25 ± 0.02
TR biomass (0.1%)	2.112×10^{-8}	1.552×10^{-11}	12.4 ± 0.5	0.25 ± 0.01

Note: ± SD – standard deviation; **Parameters:** G – water vapour flow rate [kg s^{-1}]; δ – water vapour permeability [kg m^{-1} s^{-1} Pa^{-1}]; μ – water vapour diffusion resistance factor [-]; s_d – water vapour diffusion-equivalent air layer thickness [m].

The water vapour diffusion resistance factor (μ) indicates the degree to which moisture is transferred between the exterior and the interior surfaces. The results between all the formulations were similar, although the formulations containing natural fibres showed a slightly higher moisture transference capability, as referred to in another study [135].

-1 -1

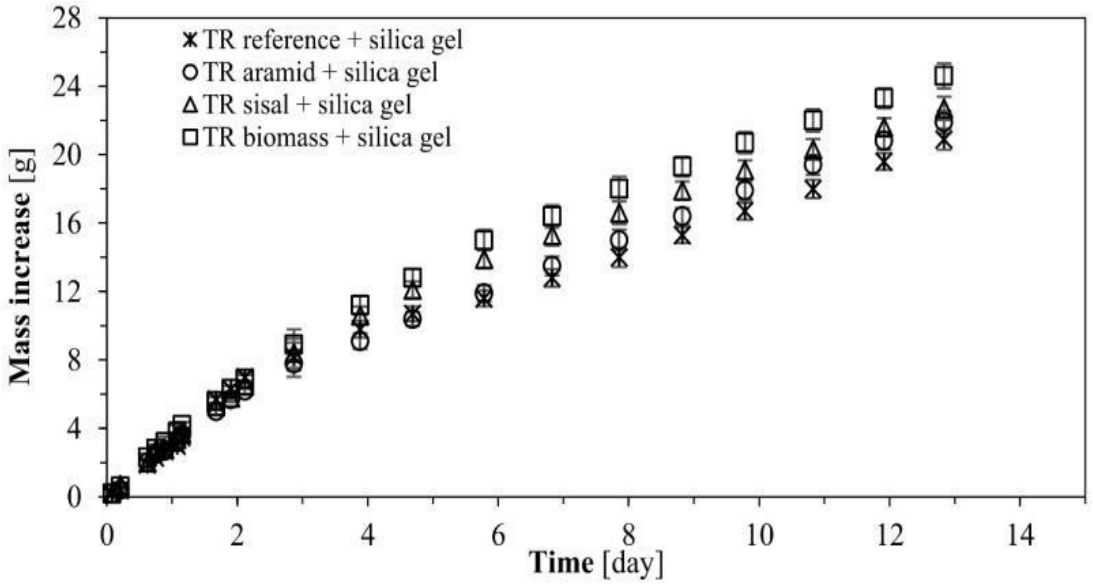

Figure 11. Average mass increase with time for each formulation. Error bars show the standard deviation for each

Here, it would be expected that the water vapour permeability showed higher variability in the results, due to the porosity differences, as well as the water and vapour affinity of the natural fibres; however, that was not verified. This fact can be related to the specimens' production which can influence the finishing of the surfaces and influence the results [136]. Nonetheless, the results show that the values are within the ones shown by other TRs [124], being slightly higher than other aerogel-containing plasters [137,138] but much lower than other thermally insulating materials (*e.g.* EPS and XPS) [94,139].

Sorption and desorption measurements using the DVS technique were made for small samples of the powder and paste (without silica aerogel granules) and the aerogel and the fibres, with the results presented in

Figure 12.

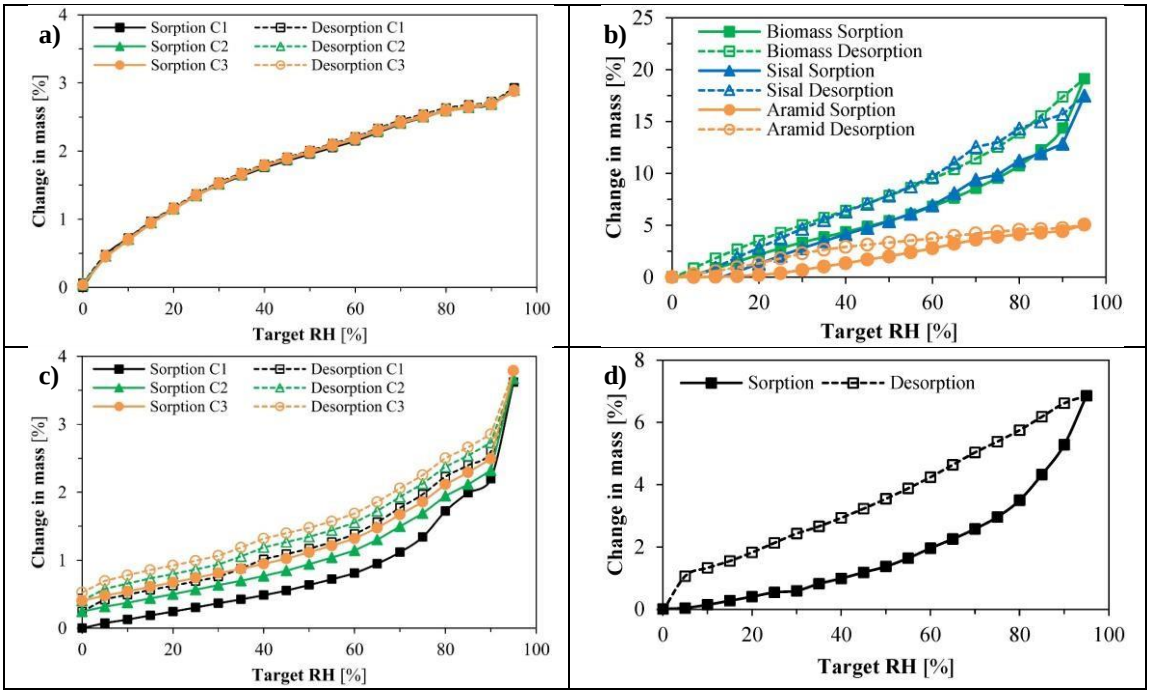

Figure 12. Dynamic vapour sorption **(**DVS) results: a) silica aerogel; b) fibres; c) powdered render; d) render paste in the hardened-state

The silica aerogel analysis,

Figure 12 a), showed no hysteresis and that, as expected due to the hydrophobic treatments that it has, the change in mass was below 3% for 95%RH. When the fibres are analysed,

Figure 12 b), both natural fibres (sisal and biomass) showed higher changes in mass than aramid (almost 15% difference). As the render in the hardened-state showed a maximum hysteresis value of 2.5%, in comparison the biomass fibres showed a value of 3.3%. The higher hysteresis of the natural fibres was expected [140], due to their known higher moisture affinity. This is an interesting characteristic to consider for application in situations where moisture buffering is required [141]. Although the biomass fibres do not yet present known values, the sisal fibres already have their behaviour characterised in other studies, Xie *et al.* [142], reported maximum mass change values of ≈ 12%, which is lower than the value verified (≈ 17%). This factor can result from the heterogeneity associated with natural fibres, which reflects in different levels of performance. The aramid fibres, which are similar to Kevlar and have a known behaviour [142–144], exhibited a similar trend with an identical maximum change in mass

values (less than 5%). The aramid fibres showed less change in mass than the natural fibres due to their lower water affinity [56] when compared with the natural fibres [69,145].

When the powder was analysed for three sorption and desorption cycles,

Figure 12 c), a significant increase in the sample's mass, even in cycles 2 and 3 is observed from 75 to 80% RH. This result shows that the powder presents significant moisture uptake in higher relative humidity values. Whereas after mixing with water and curing for 28 days (*i.e.* hardened-state),

Figure 12 d), the paste without the silica aerogel, although presenting a significant mass change due to moisture during the cycle, could return to its initial state, without significant hysteresis.

3.5. Microstructural characterisation

To observe the scatter and orientation of the fibres, the interior surfaces from prismatic samples, for each fibre type enhanced render, were observed under an OM (50x). Figure 13 highlights some noteworthy aspects identified.

From the different formulations, all the specimens showed similar aspects: fibres homogeneously scattered in the specimen's section and randomly oriented in relation to its largest length. At this observation scale, the fibres showed bonding with the matrix, and this was also verified when they were manually pulled off from their matrices. When compared with the results from previous works [35], it can also be seen that the fibres did not influence the aerogel distribution in the matrix.

The MIP technique allows characterising the open porosity above 1×10^{-2} μm. With such a technique, it was possible to obtain the results presented in Table 12 and Figure 14.

In Figure 14, the bottom graph represents the cumulative pore volume, and the top graph represents the derivative distribution of pore diameters. The most significant differences between the formulations appear above a pore diameter of 5 μm (macropores, following IUPAC's classification [97]). The dashed red line at 10 μm indicates the limit between capillary pores (below 1 μm) and air voids (above 10 μm), with capillary pores (0.002 to 10 μm) being considered the main spaces where percolation occurs [102].

When the total pore area and the porosity were analysed, the use of natural fibres slightly increased the porosity, but it was reduced by 1.20% in the aramid-containing formulation. For both the critical and threshold pore diameters, fibre use led to a reduction of their diameters compared with the reference, most noticeable in the aramid

formulation. These results show that the fibre-containing formulations reduced the available diameters of the percolation network.

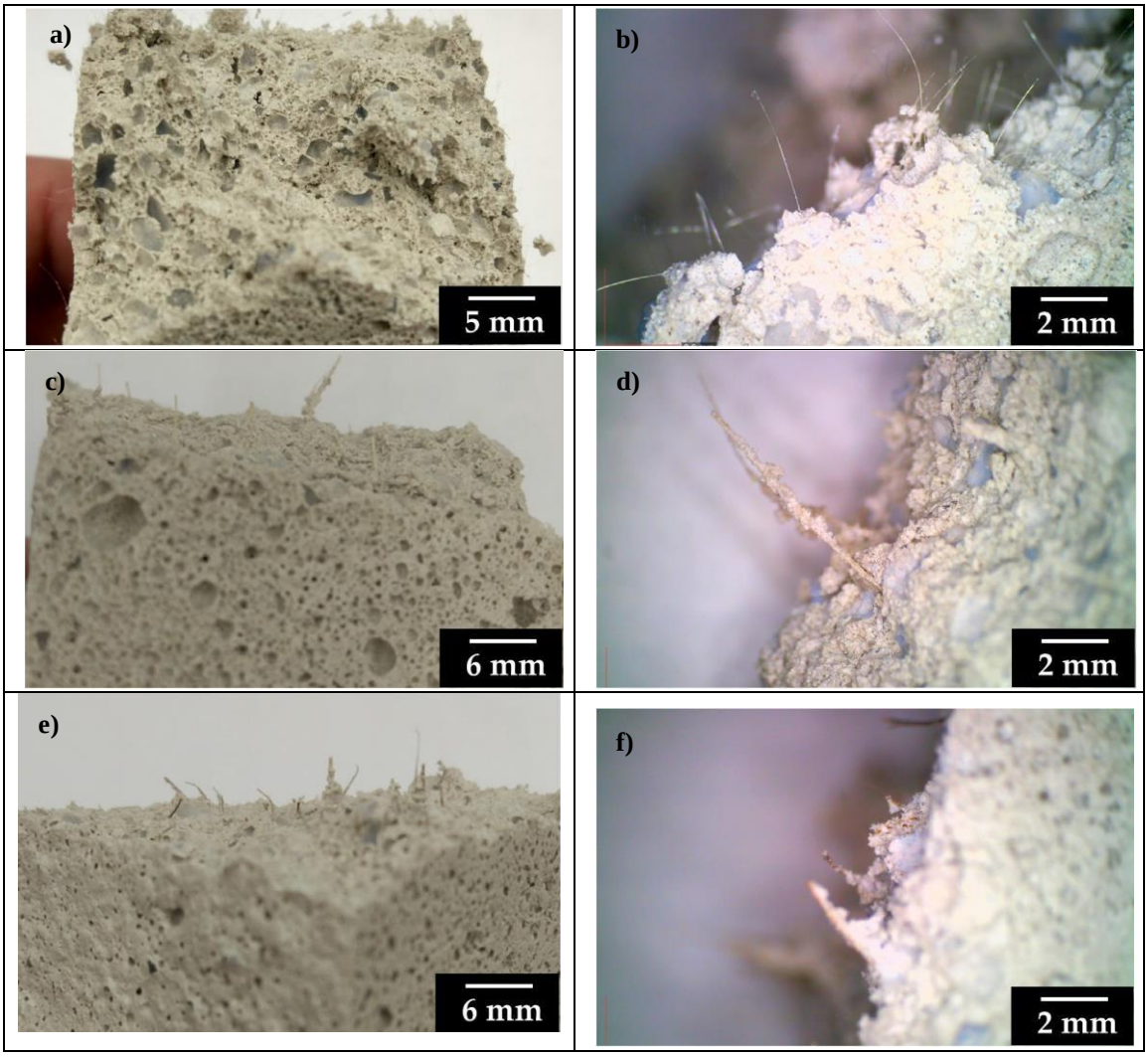

Figure 13. Fibre distribution observation on the specimens: a) and b) TR aramid; c) and d) TR sisal; e) and f) TR biomass

When Figure 14 is further analysed, the fibre-containing formulations show a first small peak/plateau before the main peak. This fact can correspond to the pressure required to break through blockages in the capillary pore network [146], such as the presence of fibres. The same Figure shows that for the differential graphic, the fibrecontaining formulations showed lower quantities of pores below 10 μm, impacting their characteristics of water percolation. It can also be seen that the fibres' use increased the volume of pores above 20 μm over the reference, which can be related to air-entrained when the fibres are being mixed with the powder and the water [12], and to their shrinkage after a water loss, most significant in the natural fibres.

Nonetheless, the application of this technique to these formulations must be considered in the context of some known limitations: as the test needs a small-sized sample, and the pore structure is heterogeneous, it can lack representativeness of the material [146]; when obtaining a sample, the researcher can affect its morphology due to involuntary crushing [147]; if closed pores are present in the material, some of these will be broken open, influencing the volume of pores [148]. In this specific case, since the formulations present high porosities and low modulus of elasticity, they can fracture and suffer dimensional changes when subjected to high pressures, relative to the material properties [149], changing their pore characteristics [150].

Table 12. Results of the MIP technique

Render designation	Sample mass [g]	Total pore area [m^2 g^{-1}]	P_0 _ Open Porosity [%]	Critical pore diameter [μm]	Threshold pore diameter [μm]
TR reference (0.0%)	0.169	65.3	86.3	8.63	20.0
TR aramid (0.5%)	0.172	67.0	85.1	8.21	14.0
TR sisal (0.1%)	0.176	64.6	86.9	7.50	15.0
TR biomass (0.1%)	0.156	66.5	87.0	6.90	16.5

Note: Mercury contact angle of 140 degrees and an equilibration time of 40 s were used.

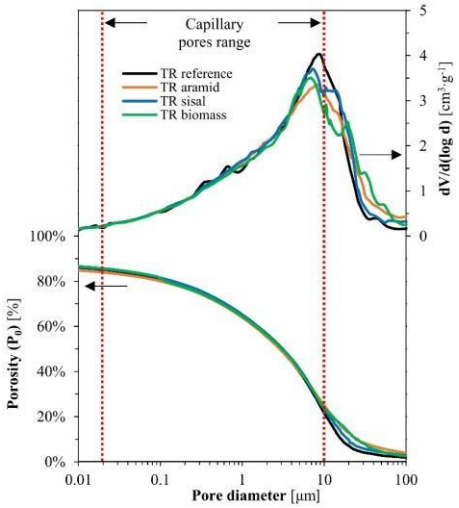

Figure 14. MIP cumulative and derivative curves (dashed red lines: capillary pores range)

In Table 13, the BET technique results can be seen for all the samples. The table also presents the values of the lightweight aggregates used in the aerogel-based thermal insulating render's formulation, as a reference. As it can be seen, the *C* parameter for all samples is between 5 and 150 [97], therefore satisfying the previously mentioned conditions of applicability.

For the aerogel-based fibre-enhanced thermal insulating renders, the N_2 adsorption/desorption isotherms at 77 K curves are shown in Figure 15 a). These isotherms are classified as type *IIb* [97,152,153] and agree with results presented by Júlio *et al.* [151] and with Pedroso *et al.* [35] for the aerogel-based render. Thus, at this evaluation scale, the pore structure is determined by the lightweight aggregate and fibres (due to their structure), either because of their characteristics or the amount used in the formulation. When the lightweight aggregate characteristics are verified (Table 13), it is possible to see that the total pore volume (V_P) owes a significant part of its performance to the silica aerogel. Here, both TR sisal and TR biomass kept a similar behaviour to TR reference. However, the TR aramid formulation showed a lower V_P, with the higher quantity of aramid fibres used (0.50% *vs* 0.10%) and reduced dimensions being a potential reason for such behaviour.

Table 13. Results obtained through N_2 isotherms at 77 K

Render designation	**m** [g]	**S** [m^2 g^{-1}]	**C_{BET}** [-]	**V_P** [cm^3 g^{-1}]	**ϕ^{BJH}** [nm]
TR reference (0.0%)	0.2650	274.4	21.2	1.319	16.77
TR aramid (0.5%)	0.2360	208.1	20.7	1.004	16.74
TR sisal (0.1%)	0.2618	266.2	20.5	1.312	16.93
TR biomass (0.1%)	0.2181	274.2	20.7	1.321	17.00
Aerogel [151]	-	698.0	15.0	2.500	11.20

$_2$ $^{-1}$

_ mean mesopore diameter obtained by the BJH method [nm].

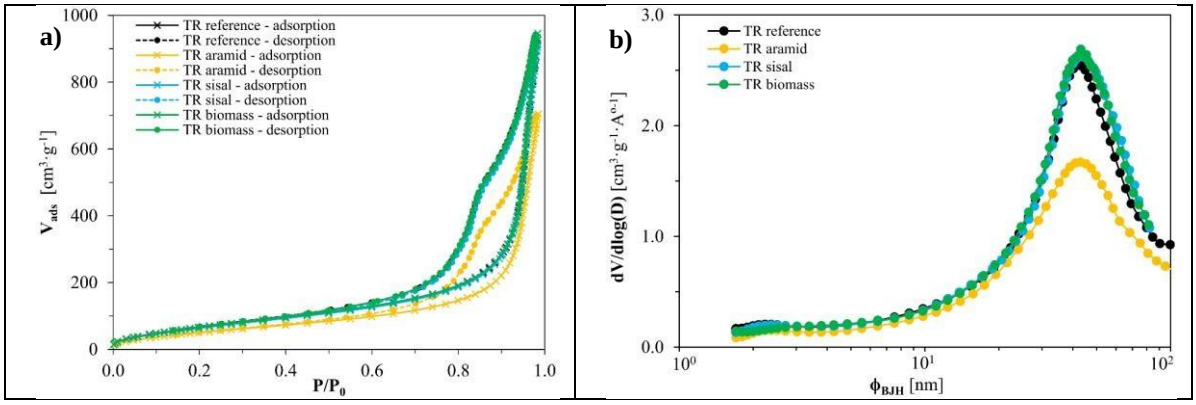

Figure 15. Surface area results: a) BET N_2 adsorption-desorption isotherms at 77 K; b) BJH mesopore distribution

Figure 15 b represents the distribution of the formulations' mesopore size. There, the existence of mesopores from 2 nm onward is verified. In addition, there is an increasing concentration considering mesopores with a dimension

Note: m – sample mass [g]; S – specific surface area [m g]; C_{BET} – BET constant [-]; V_P – total pore volume [cm^3 g^{-1}]; ϕ_{BJH}

of 10 nm (mesopores consistent with the mean value of aerogel - Table 13). Also, the average mesopore size for all formulations continues to be relatively close to that of aerogel (≈ 40 nm) [154]. All formulations, except for the TR aramid, maintained a similar behaviour to the TR reference. The higher densification and number of fibres of the TR aramid (see SEM and MIP) seem to reduce the associated volume of mesopores.

As it is known, the existence of mesopores influences the heat transfer [154] because, with the presence of a higher volume of mesopores of smaller dimensions, the convection and conduction paths of gases are significantly reduced, only remaining radiation and conduction (through paste and aggregates) as transmission factors [155–157]. Therefore, this fact can also influence the higher thermal conductivity that TR aramid shows, where not only the fibres contribute but also its mesoporous structure shows its effect.

SEM analysis was used to visually access the formulations' microstructure. Here, it was possible to see that the fibres significantly influenced the microstructure of the render. Figure 16 a) shows that the aramid fibres were distributed around the aerogel granules while also showing good bonding with the matrix. This is observed through the interfacial transition zone (ITZ), Figure 16 b), usually considered as a value below 5 μm [150,158]. When observing Figure 16 a) more carefully, it can also be seen that the fibres filled and obstructed some of the available pores and capillaries, which can influence the water transportation phenomena.

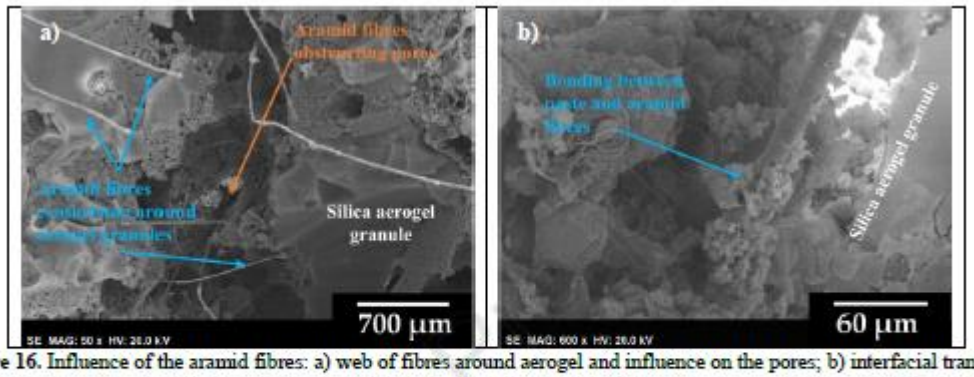

Figure 16. Influence of the aramid fibres: a) web of fibres around aerogel and influence on the pores; b) interfacial transition zone (ITZ) fibre matrix with good bonding

At the same time, both natural and synthetic fibres served as anchors, Figure 17 a) and b), and are one of the contributions to the composites' mechanical performance.

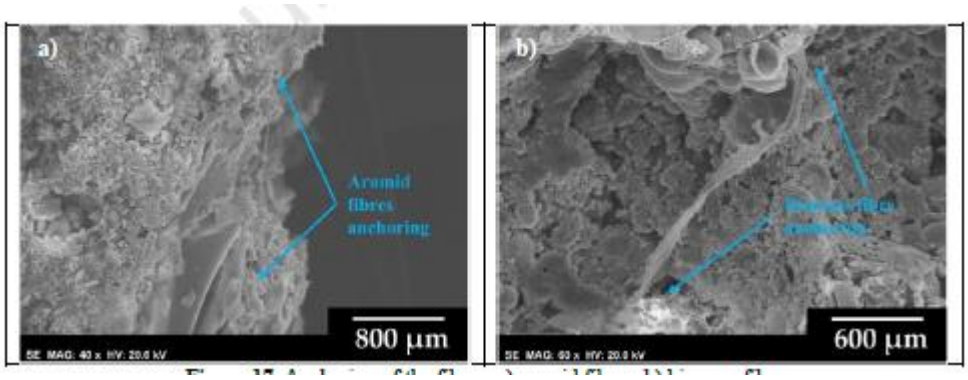

Figure 17. Anchoring of the fibres: a) aramid fibres; b) biomass fibre

In Figure 18, the presence of voids around the natural fibres was observed. This behaviour was already expected since these fibres show high water absorption values (Figure 5), which influences their diameter [159] when saturated or dried, impairing a uniform distribution. When they dry, they retract and partially detach from the matrix, explaining their low contribution to improving the composites' mechanical performance. Figure 18 a) shows air voids' presence not interconnected, which serves as one more way to resist water transportation.

Furthermore, Figure 18 b) also shows that the binders bond with some of the fibre's perimeter, which can contribute to the improvement of the composites' mechanical performance. This is linked with the formation of the previously mentioned reinforcement web.

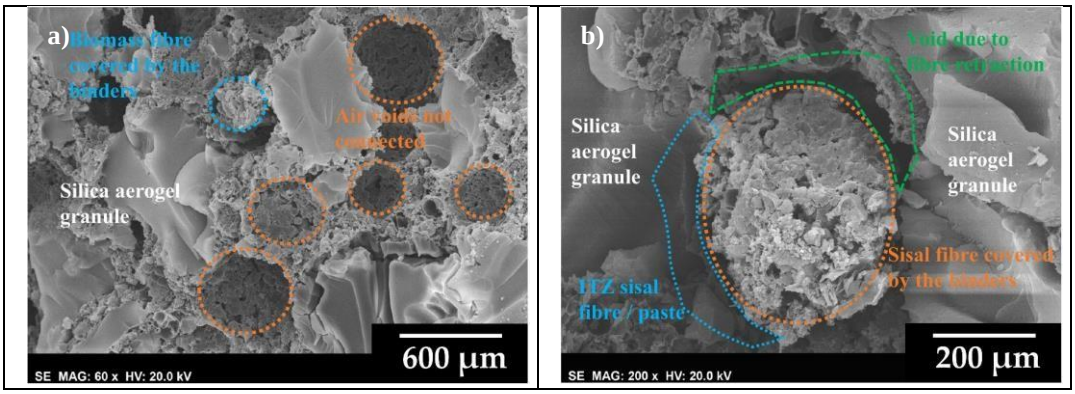

Figure 18. Natural fibres ITZ and voids: a) air voids and biomass fibre; b) ITZ of a sisal fibre

Finally, an analysis was made to characterize the molecular structure of several small samples, where their average spectra were further studied. For this analysis, the spectra were superimposed while also being normalised to their maximum of the ν_{as} Si-O-Si band, allowing comparison of the different formulations.

As these formulations include natural and synthetic fibres, their spectra were analysed before analysing the TR formulations. The natural fibres, which are comprised of cellulose, have typical spectra available in the literature.

However, the aramid fibres, usually related to polyamide, have limited relevant data regarding their spectra. Therefore, a more in-depth analysis of the aramid fibres was required.

The usual DRIFT spectrum for cellulose and the other usual constituents of vegetable natural organic fibres (*e.g.* lignin and hemicellulose) are widely known and published in research works [107]. Therefore, it is known that it usually presents two strong broadbands: one at about 1080 cm^{-1} due to C-O and the other at about 3300 cm^{-1} due to the O-H groups [107]. Since cellulose is a polysaccharide [160], it also shows a moderately strong band at 1620 cm^{-1} that is partially associated with intramolecularly bound water and partially due to the presence of a carboxyl group [107].

The aramid fibres are included in the family of polyamides (one known material in this group is nylon). The spectrum most widely known is related to Nylon-6,6 [109]. The spectrum for such material is characterised by presenting a single N-H stretch around 3300 cm^{-1}, a carbonyl C=O stretch at 1641 cm^{-1}, and an N-H bend at 1541 cm^{-1} [109,161]. When

Figure 19 a) is observed, it can be seen that the aramid fibre spectrum, which was pulled from the render sample and could have some contamination, showed similar behaviour to Nylon 6,6, with the same characteristic bands in evidence, with these factors possibly indicating the good bonding between fibres and paste. Moreover, in

Figure 19 a), it is seen that the aramid fibres influenced the TR aramid formulation over TR reference due to the aramid fibre contribution.

When all spectra obtained for the different thermal insulating render formulations are compared,

Figure 19 b), the TR reference results remained stable (when compared with previously published results [35]), indicating the chemical reproducibility of the formulation.

The global observation of

Figure 19 b) shows that the concentration of aramid fibres in the TR aramid (using 0.50% vol.) formulation is sufficient to identify its presence in the sample spectrum: by increasing the intensity of some bands or the appearance of shoulders in the positions of characteristic bands associated with the aramid, over TR reference, as it can be verified in

Figure 19 a). As for the natural fibres used in the studied formulations (TR sisal and TR biomass), due to their low concentration (0.10% vol.), a significant contribution of their use over the spectrum of TR reference was not observed

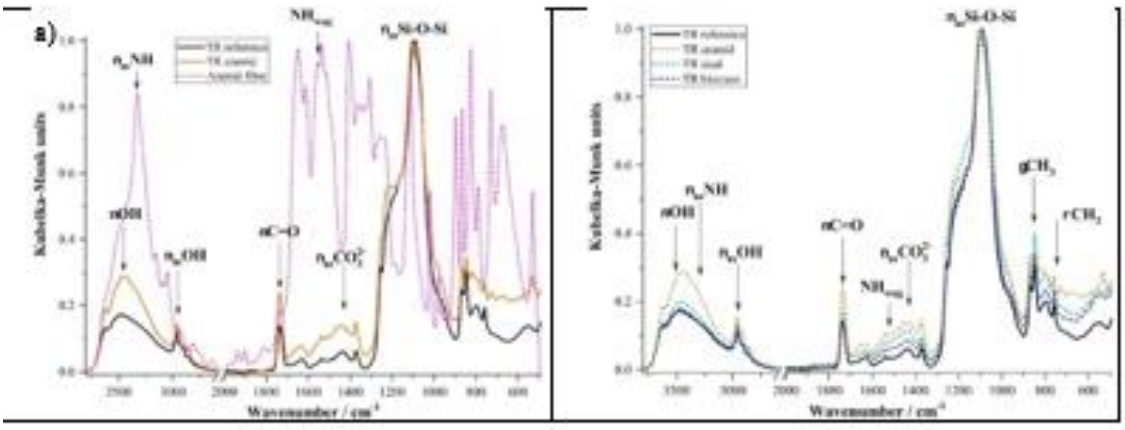

Figure 19. DRIFT spectra: a) aramid fibres over TR reference and TR aramid; b) all thermal render formulations

When the spectra of the thermal insulating renders are analysed and compared with the analysis previously made [35], it can be seen that the band in the region between 3750 and 3250 cm^{-1}, which results from O-H elongation vibrations, was present for all the formulations except for the TR aramid, indicating the involvement of residual silanol groups in hydrogen bonds, but also including contributions from hydroxyl groups originated on the paste and adsorbed water [151]. The TR aramid showed an increase due to the N-H stretch verified for the aramid fibres.

The spectra,

Figure 19 b), shows characteristic bands attributed to -CH_3 modes: ν_{as} (at 2960 cm^{-1}), γ (at 849 cm^{-1}) and ρ (at 757 cm^{-1}), with these organic groups associated with the aerogel hydrophobisation [157,162], and the resin present in the formulations [109]. The peak at around 1700 cm^{-1} is assigned to the C=O stretching mode, associated with the organic portion of the elements present in the formulations, where using aramid fibres increased it [110].

The effectiveness of the binder hydration and subsequent carbonation reactions can be verified through the band's presence identifying the asymmetrical elongation (around 1400 cm^{-1}) ν_{as} CO_3^{2-} [108]. Here, it seems that the use of all fibres contributed to its increase, which can be related to the decrease of capillaries that promote the exit of liquid water from the render microstructure (seen in the SEM and MIP tests). This fact can also play an important role when it is seen that at around 500 and 750 cm^{-1}, some peaks related to tricalcium and dicalcium silicates and tetra calcium aluminoferrite present in Portland cement [163–166] can be identified. These were more substantial in the fibre-containing formulations, indicating added hydration reactions. Nonetheless, the aramid fibre contribution seems to increase the TR aramid contribution for those bands due to its characteristic band

distribution. Finally, at around 1090 cm^{-1} the asymmetrical elongation of the siloxane bridges, ν_{as} Si-O-Si, associated with the silica aerogel and the silicates present in the formulations [106,167], can be identified.

4. Critical analysis of the results

4.1. Fibres

The analysis found that the natural fibres presented higher diameters and lower densities than the synthetic ones, as expected [141,168]. As for their morphology, the aramid showed a smoother surface than the natural fibres, with a lower diameter and higher density. When the water absorption was evaluated, it was verified that the natural fibres, due to their hydrophilic nature, presented much higher values than the aramid (≈ 300% *vs* 3% of mass increase by water absorption, after 48 hours).

4.2. Fresh state

For the fresh state, the introduction of synthetic fibres had more influence on the decrease of the workability, consistency, and air content, and in the increase of bulk density than the natural ones. However, all values were kept within the desired ranges of workability and consistency. The aramid fibres' behaviour can also be related to their higher incorporation volume (0.50%), but also to the higher number of fibres that, for the same volume, are present in the mix due to their lower diameters (10 times less) [169].

One of the needs related to the use of aerogel granules, due to their lightweight and hydrophobic nature, is the presence of admixtures in the formulations, increasing air content, and allowing the mixing of the aerogel with the paste [28,30], while also contributing to their dispersion in the render [170]. This led to the water to powder ratio of 1.30 (m/m). Initially, due to the high water absorption of the natural organic fibres, it would be expected that this would negatively impact the render's workability and consistency. However, this was not verified since a high free water quantity was maintained. To better understand this, considering that 100 g of powdered render will require 130 g of water and that each gram of biomass fibres can absorb 3.53 g of water, even if 2.00% (vol.) of fibres are used, ≈ 93 g of water would remain available. As the render has ≈ 40 g of binder per 100 g, this would result in water to binder ratio of 2.32, well above the minimum of 0.42 [101,171].

For the fresh bulk density, as the silica aerogel particles represent ≈ 70% (vol.), with a bulk density of ≈ 90 kg m^3 [15], low values were expected. This was achieved for the natural fibres (presenting density values above 700 kg

m^{-3}), while the aramid fibres, due to their higher density (densities above 1440 kg m^{-3}) and used quantity, led to a 5% increase. This behaviour is usually not verified in conventional cement-based composites due to the fibres' densities being lower than, for example, a sand and cement mortar, which in the fresh state can present values around 2000 kg m^{-3} [172]. The air content increased for the natural fibres (+ 1%), which can be due to air formation around these fibres in the mixing process and the presence of air in their structure [120,173]. In contrast, aramid fibres affect the matrix density of the render because fibres filled and obstructed pores and capillaries, serving as anchors (already seen in Figures 16 and 17). The open porosity of TR aramid is the lowest (around 85%, Table 12).

4.3. Mechanical characteristics

After 28 days, the compressive and flexural strength of TR reference were similar to those results of previously reported investigations [35,39], with a small variation of results (≤ 15%). However, the inclusion of fibres had a considerable influence on the overall hardened-state performance.

When the bulk density was tested, low values were expected due to the high water content needed for mixing, much higher than the one needed for the chemical reactions, which is then lost by evaporation, leaving voids and channels; but also due to the intrinsic low bulk density of the silica aerogel. However, an interesting behaviour was registered since fibres' insertion in cement-based composites usually leads to lower densities [12], but this was not the case. Due to the minimal amount of used fibres (aramid with 0.5% (vol./vol.), and sisal and biomass with 0.1% (vol./vol.)), only the formulation with aramid showed a slight increase in bulk density. This can be related to the higher density associated with those fibres (1440 kg m^{-3} [116]) since the higher presence of aerogel (≈ 70% (vol.)) and its very low bulk density (≤ 90 kg m^{-3} [55]) are the main influencing factors on the overall bulk density when the substitution of volume occurs. Compared with other aerogel-containing formulations (≈ 200 kg m^{-3} [123,174]) already available on the market, these formulations presented lower bulk density values even with the fibre's addition. Moreover, if compared with other thermal insulating renders (> 250 kg m^{-3} [18,175]), it also shows a significantly lower value.

Although there was a significant loss of water (fresh *vs* hardened bulk density) that could lead to cracking [33], there were no visible cracks during the specimens' unmolding. As it is also known that the inclusion of fibres is usually associated with improved behaviour in this problem [176], it seemed that the same behaviour was

maintained for this formulation. This could also be related to the low dynamic modulus of elasticity that, as it will be seen, could allow some deformability capacity [20].

For the dynamic modulus of elasticity, it was verified that it decreased (by 4%) for the natural fibre formulations, but for TR aramid, it significantly increased (by 50%). Even with that increase, these values are still well below other TRs (≈ 500 MPa [20]), which translates into higher capacities of deformation [177]. Therefore, the addition of fibres maintains the initial characteristics of good deformation potential, allowing the solutions to move along with the expansions and retractions of the support, preventing the appearance of cracks. All fibre-containing formulations showed a higher capability to deform while holding some stress after their peak compressive strength was surpassed (above a 4 to 5% strain).

However, problems in the ITZ between fibres and matrix can justify the decrease in compressive strength [12], mainly on natural fibres. Nevertheless, as stated in previous research [12,178], when reducing the diameter, length, and volume fraction of fibres, mechanical improvements can be obtained even for natural fibres. With these considerations, fibre use led to variations in mechanical improvements in both compressive and flexural strengths (12% and 80%, respectively), depending on the type of fibre. The results presented show that while aramid fibres generally provide improved mechanical performance at the expense of insulation (but with a slight effect), organic fibres have a negligible or sometimes even minor negative effect on mechanical properties.

Another interesting behaviour of the addition of aramid fibres was the type of rupture: while the reference was brittle, with the aramid fibres, it was possible to maintain some internal cohesion, being more ductile, with a similar behaviour being verified in the flexural strength test, where even after the end of the test the two halves were still connected. The improvements over TR reference were not significant for the natural fibres, possibly maintaining or slightly improving (by 3%) some mechanical properties.

When the adhesive strength was studied, it was seen that the natural fibre formulations did not improve the reference result, being only improved by the formulation containing the aramid fibres (by 13%). It could also be seen that all renders showed good bonding with the basecoat since the results of the adhesive strength and rupture type were maintained. As for the impact, only TR aramid showed significant improvements over the reference in both 3 J (less 5%) impact and pendulum hammer index (more 5%), indicating improvements in the formulations' shock resistance.

4.4. Physical characteristics

When considering the thermal properties, the fibre incorporation, due to their higher thermal conductivity, increased the overall thermal conductivity in the dry-state, but less than 7% relative to the reference, and still below EPS ($\lambda_{10^{o}C} \approx 0.036$ W m^{-1} K^{-1} [126]). This was an interesting aspect since the introduction of natural fibres in cement-based composites is usually linked with thermal conductivity lowering due to increased porosity and lower thermal conductivity of the fibres *vs* the paste [12,54]. In this case, as the silica aerogel has a low thermal conductivity, this usual behaviour was not verified.

As for the capillary water absorption, the incorporation of fibres led to lower water absorption coefficients while also changing the capillary water progression. TR reference showed a stronger capillary network, enabling rapid water progression through the material, while the samples with fibres, after an initial phase with a fast capillary transport, quickly changed to a slower water progression. As seen through the MIP and SEM results, the fibres cut some of the capillaries, slowing down the water absorption [128]. When comparing the performance between the fibre-containing formulations, it is seen that the TR aramid formulation showed a lower water absorption, with this behaviour being expected as aramid shows much less affinity to water than the natural fibres.

When considering the drying properties of the formulations, it is known that both capillary water absorption and water vapour permeability influence the overall performance [95]. The formulations lowered their capillary water absorption with fibre use while presenting higher water vapour permeability. This way, it was possible to obtain a slightly lower DI. The most significant difference between the fibre-containing formulations and the reference was the shift between the knick-point, which can be related to the stronger capillary network of the reference. As for the differences between fibres, due to the higher water affinity of the natural fibres compared to aramid, more time was required for drying.

The water vapour permeability showed low variability in the results between the TR reference and the fibrecontaining formulations. Nonetheless, the formulations with natural fibres showed a slightly higher moisture transference capability, although a higher level of influence on the results was expected. This can be related to the surface finish which can influence the results [136].

As seen through the DVS test, the powder showed a high affinity to moisture. This is a relevant factor to consider when shipping such a product since from 75%RH onward, the powder showed an increase of mass without losing

weight in subsequent cycles, indicating the existence of binder hydration reactions. Therefore, care should be taken when designing its package, where materials that protect the powder from moisture should be applied. The silica aerogel did not show any significant water absorption, as seen in its lack of hysteresis. As for the paste, it also presented considerable hygroscopic behaviour (6% variation) with a significant contribution of the natural fibres (change in mass above 15%), since aramid showed less absorption than the paste; therefore, the similar hygric behaviour between all the formulations seems related to the paste. However, when tested the over-hygroscopic range (capillary water absorption), it started to show differences, with less water absorbed by the fibre-containing formulations, either by reducing capillaries or reducing pores linked to the exterior [12,128,179]. Here, once again, the TR aramid formulation was showing less water absorption than the remaining formulations.

4.5. Microstructural characteristics

The microstructural analysis allowed an understanding of the different behaviour previously observed. With the use of fibres, it was reasoned that it would be possible to improve the renders' mechanical performance due to the multiple orientations of low diameter fibre strands that could form an effective web of reinforcement around the aerogel granules, which would allow the composite to resist crack propagation [43]. As for the natural fibres, it was expected that they relied on their irregular and uneven surfaces to provide several anchorage points in the matrix [159,180].

From all the studied fibres, aramid had the smoothest surface [181], with the natural fibres showing much more irregular surfaces and varying diameters due to water absorption and release [51]. The biomass fibres showed a lack of fibre individualisation and the presence of some extractives even after the chemical treatments [182]. These facts seem to be related to their lower performance, which can potentially be improved if the small fibres, seen through SEM, are industrially treated and individualised.

With the OM, it was possible to see that the fibres, in all cases, were homogeneously scattered all around the specimen's limits while also being randomly oriented. The formation of fibre clumps which are known for their negative influence on the composites' mechanical properties was not identified.

With both the MIP and the SEM results, it could be seen that the presence of the aerogel increased the kneading water quantities to allow adequate workability, being a consequence of its hydrophobically treated surfaces [28] but also to the presence of rheological agents required to disperse the aerogel granules [157]. This need for higher

water quantities led to higher porosity values [23,35], being one of the main influences on the composites' mechanical and physical performance [101].

Since it is known that high porosity is usually related to lower mechanical performances [183,184], with the introduction of fibres, two different scenarios emerged. The aramid fibres reduced the open porosity, while the natural fibres increased it. The aramid fibres did not present significant hygroscopic behaviour, contributing to a higher compacity, and at the same time, they showed good adhesion to the matrix seen through SEM images showing the ITZ fibre/matrix. As for the sisal and biomass fibres, due to their known water affinity [69], they soak water in the mixing phase, increasing their volume. When the render dried, the fibres lose water, decreasing their volume and detaching from the matrix while making it more brittle [185,186], resulting in interior air voids [12,187] and influencing the open porosity, as seen in the SEM images. However, it was also seen that half of the natural fibres' perimeter remained connected to the matrices, which can also relate to the slight increase in their mechanical performance. Therefore, the hypothesis of a structure formation, like a net around the aerogel granules, and at the same time, the fibres' anchoring to the matrices, was verified. Another aspect observed was the reduction of mesopores (seen in the BET) for the TR aramid formulation, which can be an added factor for this formulation's higher thermal conductivity.

Also, the results of the hygric properties of the fibre-containing renders showed that there was a positive influence on the renders' properties. As MIP, SEM, and BET showed, the fibres reduced the quantity of pore diameters linked to capillary pores related to water transport. This fact was also shown in SEM images since some fibres were seen inside some capillaries hindering the water movement. Although the natural fibres are hydrophilic, they did not increase the capillary water absorption due to their smaller length and formation of non-connected air voids.

When the molecular properties of the formulations are analysed, it can be seen that the use of fibres promoted more chemical reactions associated with the hydration of the binders (cement-based), mostly seen in the region between 500 and 750 cm^{-1} [164]. Although initially, there is plenty of water available for the binder hydration reactions, the use of admixtures can potentiate a lower degree of hydration due to air entrapment [188,189]. Here, the use of fibres (natural and synthetic), as seen in the SEM, MIP and BET analyses, influenced the microstructure of the formulations, reducing capillaries, which possibly made water available for a longer time. Also, natural fibres are linked to a certain “water container” effect, which can influence such delayed hydration [12,186,190]. Nonetheless,

although the aramid fibres do not store water (as seen through the various analysis made), they influenced the microstructural arrangement of the TR formulations, which can also impact such delayed hydration phenomena (this could be seen in a slower rate of drying in the drying test). Therefore, the fibres' contribution allowed for the TR formulations (TR aramid, TR sisal, and TR biomass) to form more hydrates relative to the reference (TR reference). The DRIFT also showed that, for the TR aramid, and as shown in the SEM images, the bonding between fibres and paste was higher than in the other cases.

4.6. Synthesis of the results

Since several tests were carried out in this experimental campaign, the results are summarized in Table 14. In general, it can be verified that the incorporation of fibres improved the performance of renders (TR aramid; TR sisal; TR biomass) when compared to the aerogel-based render (TR reference) while losing some flow table consistency diameter and having a minor influence on the composites' thermal conductivity. The air content and elastic modulus values for organic fibres worsen over the reference. However, there are no requirements for these properties on EN 998 standard.

Table 14. Synthesis of the formulations' characteristics - average values, including standard deviation values in ( )

Evaluation	Parameter	TR reference	TR aramid	TR sisal	TR biomass
Fresh state	Water powder ratio	1.30	1.30	1.30	1.30
	Workability Cons [mm]	Excellent 143.5 (1.5)	Good 121.1 (2.3)	Excellent 139.7 (3.5)	Excellent 139.1 (3.8)
	ρ_{fresh} [kg m^{-3}]	293 (3.0)	310 (4.0)	297 (5.0)	299 (5.0)
	Air content [%]	21.5 (0.5)	19.5 (1.0)	22.0 (1.0)	22.5 (0.5)
Mechanical	ρ_{hard} [kg m^{-3}]	0.159 (3.0)	0.165 (4.0)	0.16 (3.0)	0.162 (2.0)
	$f_{c,peak}$ [MPa]	0.185 (0.002)	0.208 (0.004)	0.193 (0.002)	0.190 (0.003)
	$f_{t,peak}$ [MPa]	0.092 (0.003)	0.165 (0.012)	0.093 (0.002)	0.092 (0.002)
	Cracks during curing?	No	No	No	No
	E_d [MPa]				
	f_u [MPa]	0.066 B		0.067 B	
	$f_{u,basecoat}$ [MPa]	0.065 B (0.003)	0.073 B	Impact	
	Imp 3J ϕ [mm]	31.5 (1.5)			
	Impact cracks in 5 impacts?	3 in 5			
	Scl [-]				
	$\lambda_{10°C,dry}$ [W m-1 K^{-1}]	0.029	A_w [kg m^{-2} s$^{-1/2}$]	0.0286 (0.001)	0.0325 (0.0011)	0.031 (0.0013)
		0.109				
	C [kg m^{-2} min$^{-1/2}$]	0.90			
	D1 phase [kg m^{-2} h^{-1}]	0.172 (0.011)	0.147 (0.012)	0.159 (0.015)	0.162 (0.014)
	D2 phase [kg m^{-2} h$^{-1/2}$]	1.483 (0.021)	1.485		
	DI	0.20 (0.01)	0.19	μ [-]	
		13.7			
	P0 [%]	86.3			

Legend:
Improved over reference
Similar or non-significant
Worsen over reference

Note: Cons – flow table consistency [mm]; ρ_{fresh} – bulk density fresh state [kg m^{-3}]; ρ_{hard} – bulk density hardened-state [kg m963 ^{3}]; $f_{c,peak}$ – compressive strength peak value, maximum value [MPa]; $f_{t,peak}$ – flexural strength peak value, maximum value 964 [MPa]; E_d – dynamic modulus of elasticity [MPa]; f_u – adhesion [MPa]; $f_{u.basecoat}$ – adhesion between render and basecoat

[MPa]; Imp 3J ϕ – 3 Joule sphere impact diameter [mm]; Scl – PT pendulum hammer hardness index [-]; $\lambda_{10ºC,dry}$ – thermal conductivity at 10 ºC and dry-state [W m^{-1} K^{-1}]; A_w – capillary water absorption coefficient [kg m^{-2} $s^{-1/2}$]; C – capillary water absorption [kg m^{-2} $min^{-1/2}$]; D1 – D1 drying phase [kg m^{-2} h^{-1}]; D2 – D2 drying phase [kg m^{-2} $h^{-1/2}$]; DI – drying index; μ – water vapour diffusion resistance factor [-]; P_0 – open porosity by MIP [%].

The influence that the fibres presented was related to the microstructural aspects previously seen, in which the fibres created nets surrounding the aerogel granules, improving the mechanical parameters while, at the same time, influencing the composites pore structure and reducing the liquid water absorption. The distribution and orientation of fibres could impact mechanical performance. It is possible to see a higher standard deviation for flexural strength and dynamic modulus of elasticity for TR aramid when compared to the other renders (reference and R sisal and TR biomass).

Although these formulations improved the mechanical and physical drawbacks previously identified, they also kept low thermal conductivity values. In Table 15, the formulations' performance is compared with the EN 998-1 [21] requirements. The most significant overall impact of incorporating the fibres is related to a significant reduction of the capillary water absorption, where the fibre-containing formulations presented lower values than the requirements, with the reference showing 'not complying'. However, although the incorporation of fibres in the aerogel-based render significantly improved the compressive strength over the reference, none of the formulations fulfilled that requirement. This is a limitation of the study and requires further research such as optimizing the reference aerogel-based render formulation (e.g. admixtures) and evaluating renders with other fibres types and lengths to improve the interface between aerogel and fibres and increase the cohesion of the binder-matrix (porous and solid networks).

Table 15. Formulations' results and EN 998-1 [21] requirements for thermal renders

Parameter requirement	**EN 998-1** [21]	**TR reference**	**TR aramid**	**TR sisal**	**TR biomass**
ρ_{fresh} [kg m^{-3}]	Declare	293	310	297	299
Air content [%]	Declare	21.5	19.5	22.0	22.5
ρ_{hard} [kg m^{-3}]	Declare	0.159	0.165	0.16	0.162
$f_{c,peak}$ [MPa]	≥ 0.40 MPa (CS I)	0.19	0.21	0.19	0.19
f_u [MPa] and fracture pattern	Declare	0.066 B	0.075 B	0.067 B	0.066 B
C [kg m^{-2} $min^{-1/2}$]	≤ 0.40 (W1)	0.90	0.34	0.40	0.35
μ [-]	≤ 15	13.7	13.3	12.7	12.4
$\lambda_{10ºC,dry}$ [W m^{-1} K^{-1}]	< 0.100 (T1)				

Legend:

Fulfils

Non-significant
Not fulfils

Note: ρ_{fresh} – bulk density fresh state [kg m^{-3}]; ρ_{hard} – bulk density hardened-state [kg m^{-3}]; $f_{c,peak}$ – compressive strength peak 987 value [MPa]; f_u – adhesion [MPa]; C – capillary water absorption [kg m^{-2} $min^{-1/2}$]; μ – water vapour diffusion resistance factor 988 [-]; $\lambda_{10ºC,dry}$ – thermal conductivity at 10 ºC and dry-state [W m^{-1} K^{-1}].

In terms of thermal conductivity, the formulations' performance was much lower than the most restrictive 990 requirement, where the use of fibres marginally increased the results over the reference, keeping performance

similar to classic thermal insulating materials. This aspect deserves some further discussion related to the

classification of these renders, which show a hybrid behaviour between a classic thermal insulator and a current

TR.

The initial objective to improve the mechanical performance of the aerogel-based TR using fibres was partially achieved. First, higher values of compressive strength, flexural strength and dynamic modulus of elasticity were achieved, especially with aramid fibres, as well as the impact resistance (e.g. surface hardness index). Nonetheless, the compressive strength, although improving over the reference (TR reference), could not fulfil the EN 998-1 [21] requirements (TR aramid with 0.21 *vs* 0.40 MPa in the EN 998-1). This aspect deserves further discussion to evaluate if the $f_c \geq 0.40$ MPa requirement should also be used for these highly thermal-insulating innovative materials. Another aspect that significantly benefited from the fibres' use was the lowering of the capillary water absorption. This was an unexpected result, but it allowed these formulations to observe the EN 998-1 [21] requirements. Moreover, thermal conductivity, although increasing over the TR reference, continued similarly to other classic thermal insulating materials.

5. Conclusions

An experimental study assessed the main fibre characteristics and the composites' fresh state behaviour, mechanical, and physical properties while also evaluating and relating them to their microstructure and pore structure. The main conclusions of this study were:

- For the incorporated fibre types (aramid, sisal and biomass) and quantities added, the renders could maintain adequate levels of workability and consistency and simultaneously achieve acceptable dispersion throughout the volume of the specimens, with all fibres oriented randomly and not influencing the aerogel dispersion;

- Due to the heterogeneity and water absorption (> 150%, in mass) of the natural fibres, the mechanical performance improvement of the fibre-reinforced renders over the reference render was limited (by 3%), which is in line with the images obtained through the SEM analysis: fibre perimeter loss due to shrinkage after a water loss, presenting some detachment and voids in the Interfacial Transition Zone fibre/matrix;
- The smaller diameter of the aramid fibres and their low water absorption were considered the most relevant and different factor when compared with the natural fibres. When incorporated in renders, aramid fibres promoted good bonding with the matrix (as seen through SEM), potentiating their mechanical performance (> 12% over the reference for the compressive strength);
- Both types of fibres (synthetic and plant) contributed to a significant reduction of capillary water absorption (more than 50% reduction) of renders, either by reducing capillary connectivity (seen in the MIP) or by changing the render's pore structure (seen in MIP and SEM). However, they did not significantly influence the drying kinetic abilities when compared to the reference render. The use of such fibres did not significantly increase the thermal conductivity, being one of the initial objectives of keeping it within the reference values;
- As expected, a reinforcement net around the aerogel granules was formed, with the added value of the fibres also anchoring and connecting different points of the matrix contributing to load spreading, which improved the compressive and flexural strength of renders and also the impact resistance. An added benefit of the fibres' incorporation was the impact on the pore structure, reducing capillaries and hindering the liquid water transportation phenomenon;
- Overall the fibres' positively impacted the evaluated mechanical properties (compressive and flexural strength, dynamic modulus of elasticity and adhesion) over the reference (TR reference), with the advantage being to the aramid fibres (TR aramid), which seem strongly linked to their smaller size and lower water absorption, as opposed to the natural fibres. Due to their water vapour behaviour (seen in DVS results), the natural fibres, although not significantly improving the mechanical performance, can present an interesting hygrothermal behaviour. Nevertheless, between natural fibres the results are similar, the sisal fibres (TR sisal) present a marginally better behaviour than the biomass fibres (TR biomass);
- Although the fibres' introduction presented a synergistic effect on the aerogel-based TR, solving one of the main problems associated with the non-compliance of the EN 998-1 [21] requirements (capillary water

absorption reduction), the compressive strength is still lower than the requirements, even with the improvement when compared to the reference. Here, also the connections between the silica aerogel granules and the paste can improve this overall performance.

In further research, the mechanical strength of fibre-enhanced renders should be investigated for other fibre types, length, orientation and volume fractions; and for aerogel-based render formulations as reference.

The formulations based on biomass fibre require additional studies, in terms of the fibre (e.g. treatment) and of the render formulation. These should address the drying shrinkage behaviour of the fibre-enhanced renders; their response under thermal radiation cycles and their freeze-thaw resistance, particularly on composites with natural fibres, where voids due to fibre retraction and high water absorption were observed. Furthermore, the economical and environmental impact of these fibre-enhanced renders should be carried out in future investigations.

This study presents the benefits in mechanical strength and water resistance when different fibres (synthetic and natural) are incorporated in a thermal insulating aerogel-based render (without fibres). It opens the discussion of using fibres in composites to achieve a circular economy, such as the use of fibres from waste, recycled and bioproducts.

Declarations of interest

None

Credit authorship contribution statement

M. Pedroso: Conceptualization, Methodology, Investigation, Writing - original draft. **I. Flores-Colen**: Investigation, Supervision, Writing - review & editing. **J. D. Silvestre**: Supervision, Writing - review & editing.
M. G. Gomes: Supervision, Writing - review & editing; **A. Hawreen** - Writing - review & editing; **R. J. Ball**: Investigation; Writing - review & editing.

Acknowledgements

The authors wish to acknowledge Saint-Gobain Weber Portugal for making available the aerogel-based TR used in this study. The authors also acknowledge IBB – IST Prof Laura Ilharco and Prof Ana Rosa for the technical support on the BET and DRIFT tests. The authors gratefully acknowledge the support of CERIS Research Unit (UIDB/04625/2020), IST - University of Lisbon, FCT – Foundation for Science and Technology, and the University of Bath for the DVS tests and the granted internship. The first author also wants to thank FCT for PhD grant SFRH/BD/132239/2017.

References

[1] European Commission, Directive 2010/31/UE: Energy Performance Building Directive, 2010.

[2] European Commission, Directive 2012/27/EU: on energy efficiency, 2012.

[3] European Commission, Energy performance of EU buildings, (2019). https://ec.europa.eu/energy/en/topics/energy-efficiency/energy-performance-of-buildings (accessed July 15, 2019).

[4] European Commission, Long-term low greenhouse gas emission development strategy of the EU and its Member States, Zagreb, 2020.

[5] R. Baetens, B.P. Jelle, A. Gustavsen, Aerogel insulation for building applications: A state-of-the-art review, Energy Build. 43 (2011) 761–769. doi:10.1016/j.enbuild.2010.12.012.

[6] EURIMA, U-values For Better Energy Performance of Buildings - Report established by ECOFYS for EURIMA, Brussels, 2007.

[7] J. Yu, C. Yang, L. Tian, D. Liao, A study on optimum insulation thicknesses of external walls in hot summer and cold winter zone of China, Appl. Energy. 86 (2009) 2520–2529. doi:10.1016/j.apenergy.2009.03.010.

[8] A. Staszczuk, T. Kuczyński, The impact of floor thermal capacity on air temperature and energy consumption in buildings in temperate climate, Energy. 181 (2019) 908–915. doi:10.1016/j.energy.2019.05.202.

[9] M. Marwan, The effect of wall material on energy cost reduction in building, Case Stud. Therm. Eng. 17 (2020) 100573. doi:10.1016/j.csite.2019.100573.

[10] L. Perez-Lombard, J. Ortiz, C. Pout, A review on buildings energy consumption information, Energy Build. 40 (2008) 394–398. doi:10.1016/j.enbuild.2007.03.007.

[11] J. Sierra-Pérez, J. Boschmonart-Rives, X. Gabarrell, Environmental assessment of façade-building systems and thermal insulation materials for different climatic conditions, J. Clean. Prod. 113 (2016) 102– 113. doi:10.1016/j.jclepro.2015.11.090.

[12] M. Pedroso, I. Flores-Colen, The influence of dimension and content of natural organic fibrous materials on the multi-performance of cement-based composites: A statistical approach, Constr. Build. Mater. 231 (2020) 117175. doi:10.1016/j.conbuildmat.2019.117175.

[13] M. Pedroso, J. de Brito, J. Dinis Silvestre, Characterization of walls with eco-efficient acoustic insulation materials (traditional and innovative), Constr. Build. Mater. 222 (2019) 892–902. doi:10.1016/j.conbuildmat.2019.07.259.

[14] M.M. Koebel, J. Wernery, W.J. Malfait, Energy in buildings—Policy, materials and solutions, MRS Energy Sustain. 4 (2017) E12. doi:10.1557/mre.2017.14.

[15] M.R. Hall, ed., Materials for energy efficiency and thermal comfort in buildings, 1st ed., Woodhead Publishing Ltd, Abington - United Kingdom, 2010.

[16] E. Barreira, V.P. de Freitas, External Thermal Insulation Composite Systems (ETICS), Springer International Publishing, Cham, 2016. doi:10.1007/978-3-319-20382-9.

[17] E. Barreira, V.P. de Freitas, External Thermal Insulation Composite Systems: Critical Parameters for Surface Hygrothermal Behaviour, Adv. Mater. Sci. Eng. 2014 (2014) 1–16. doi:10.1155/2014/650752.

[18] J. Maia, N.M.M. Ramos, R. Veiga, Evaluation of the hygrothermal properties of thermal rendering systems, Build. Environ. 144 (2018) 437–449. doi:10.1016/j.buildenv.2018.08.055.

[19] A. Brás, M. Leal, P. Faria, Cement-cork mortars for thermal bridges correction. Comparison with cement-EPS mortars performance, Constr. Build. Mater. 49 (2013) 315–327. doi:10.1016/j.conbuildmat.2013.08.006.

[20] A. Soares, PhD Thesis in Civil Engineering: "Performance of renders incorporating nanosilica aerogels" (in Portuguese), University of Lisbon, 2018.

[21] CEN, EN 998-1: 2010 - Specification for mortar for masonry - Part 1: Rendering and plastering mortar, Comité Européen de Normalisation, Brussels, Belgium, 2010.

[22] M. Pedroso, I. Flores-Colen, J.D. Silvestre, L. Silva, P. Sequeira, G. Sousa, Development of superinsulating thermal renders: preliminary studies (in Portuguese), ICEUBI2017 - Int. Congr. Eng. A Vis. Futur. (2017).

[23] M. Pedroso, I. Flores-Colen, J.D. Silvestre, M. da G. Gomes, Nanomaterials' Influence on the Performance of Thermal Insulating Mortars—A Statistical Analysis, Appl. Sci. 10 (2020) 2219. doi:10.3390/app10072219.

[24] Nanorender, Nanorender: Performance of nanoaerogel silica-based renders (in Portuguese), (2015). http://www.florescolen.com/Documentacao/Executive_Summary(in English).pdf (accessed December 5, 2019).

[25] S. Fantucci, E. Fenoglio, G. Grosso, V. Serra, M. Perino, V. Marino, M. Dutto, Development of an aerogelbased thermal coating for the energy retrofit and the prevention of condensation risk in existing buildings, Sci. Technol. Built Environ. 4731 (2019) 1–10. doi:10.1080/23744731.2019.1634931.

[26] Saint-Gobain Weber, PEP - Efficient Plus Wall (in Portuguese), (2019). https://www.pt.weber/pep-paredeeficiente-plus (accessed December 26, 2019).

[27] Wall-ACE Project, (2019). https://www.wall-ace.eu/.

[28] M. de F. Júlio, A. Soares, L.M. Ilharco, I. Flores-Colen, J. de Brito, Silica-based aerogels as aggregates for cement-based thermal renders, Cem. Concr. Compos. 72 (2016) 309–318. doi:10.1016/j.cemconcomp.2016.06.013.

[29] S. Ng, L.I.C. Sandberg, B.P. Jelle, Insulating and Strength Properties of an Aerogel-Incorporated Mortar Based an UHPC Formulations, Key Eng. Mater. 629–630 (2014) 43–48. doi:10.4028/www.scientific.net/KEM.629-630.43.

[30] A. Soares, M. de Fátima Júlio, I. Flores-Colen, L.M. Ilharco, J. de Brito, EN 998-1 performance requirements for thermal aerogel-based renders, Constr. Build. Mater. 179 (2018) 453–460. doi:10.1016/j.conbuildmat.2018.05.197.

[31] J. Strzałkowski, H. Garbalińska, Thermal and strength properties of lightweight concretes with the addition of aerogel particles, Adv. Cem. Res. 28 (2016) 567–575. doi:10.1680/jadcr.16.00032.

[32] U. Berardi, R.H. Nosrati, Long-term thermal conductivity of aerogel-enhanced insulating materials under different laboratory aging conditions, Energy. 147 (2018) 1188–1202. doi:10.1016/j.energy.2018.01.053.

[33] P. Westgate, K. Paine, R.J. Ball, Physical and mechanical properties of plasters incorporating aerogel granules and polypropylene monofilament fibres, Constr. Build. Mater. 158 (2018) 472–480. doi:10.1016/j.conbuildmat.2017.09.177.

[34] Q. Zeng, T. Mao, H. Li, Y. Peng, Thermally insulating lightweight cement-based composites incorporating glass beads and nano-silica aerogels for sustainably energy-saving buildings, Energy Build. 174 (2018) 97–110. doi:10.1016/j.enbuild.2018.06.031.

[35] M. Pedroso, I. Flores-Colen, J.D. Silvestre, M.G. Gomes, L. Silva, L. Ilharco, Physical, mechanical, and microstructural characterisation of an innovative thermal insulating render incorporating silica aerogel, Energy Build. 211 (2020) 109793. doi:10.1016/j.enbuild.2020.109793.

[36] R. Sousa, H. Sousa, L. Silva, I. Flores-Colen, M. Pedroso, Development of a wall system made with thermally optimised masonry and super insulation mortar render, Mason. Int. 32 (2019) 3–14.

[37] M.G. Gomes, I. Flores-Colen, H. Melo, A. Soares, Physical performance of industrial and EPS and cork experimental thermal insulation renders, Constr. Build. Mater. 198 (2019) 786–795. doi:10.1016/j.conbuildmat.2018.11.151.

[38] T. Stahl, S. Brunner, M. Zimmermann, K. Ghazi Wakili, Thermo-hygric properties of a newly developed aerogel based insulation rendering for both exterior and interior applications, Energy Build. 44 (2012) 114–117. doi:10.1016/j.enbuild.2011.09.041.

[39] M. Pedroso, I. Flores-Colen, J.D. Silvestre, M.G. Gomes, L. Silva, P. Sequeira, J. de Brito, Characterisation of a multilayer external wall thermal insulation system. Application in a Mediterranean climate, J. Build. Eng. 30 (2020) 101265. doi:10.1016/j.jobe.2020.101265.

[40] EOTA, ETAG004 Guideline for European Technical Approval: External Thermal Insulation Composite Systems (ETICS) With Rendering, Brussels - Belgium, 2013.

[41] L.K. Aggarwal, Bagasse-reinforced cement composites, Cem. Concr. Compos. 17 (1995) 107–112. doi:10.1016/0958-9465(95)00008-Z.

[42] L. Rodier, V. da Costa Correia, H. Savastano Junior, Elaboration of eco-efficient vegetable fibers reinforced cement-based composites using glass powder residue, Cem. Concr. Compos. 110 (2020) 103599. doi:10.1016/j.cemconcomp.2020.103599.

[43] A.A. Belkadi, S. Aggoun, C. Amouri, A. Geuttala, H. Houari, Effect of vegetable and synthetic fibers on mechanical performance and durability of Metakaolin-based mortars, J. Adhes. Sci. Technol. 32 (2018) 1670–1686. doi:10.1080/01694243.2018.1442647.

[44] R.D.T. Filho, M.A. Sanjuán, Effect of low modulus sisal and polypropylene fibre on the free and restrained shrinkage of mortars at early age, Cem. Concr. Res. 29 (1999) 1597–1604. doi:10.1016/S00088846(99)00136-2.

[45] R.D. Toledo Filho, K. Ghavami, M.A. Sanjuán, G.L. England, Free, restrained and drying shrinkage of cement mortar composites reinforced with vegetable fibres, Cem. Concr. Compos. 27 (2005) 537–546. doi:10.1016/j.cemconcomp.2004.09.005.

[46] C. Guardia, G. Barluenga, I. Palomar, G. Diarce, Thermal enhanced cement-lime mortars with phase change materials (PCM), lightweight aggregate and cellulose fibers, Constr. Build. Mater. 221 (2019) 586– 594. doi:10.1016/j.conbuildmat.2019.06.098.

[47] B. Dams, N. Amornrattanasereegul, P. Shepherd, R.J. Ball, Cement-fibre composites for additive building manufacturing, in: R.J. Ball, B. Dams, V. Ferrandiz-Mas, X. Ke, K. Paine, M. Tyrer, P. Walker (Eds.), 39th Cem. Concr. Sci. Conf., University of Bath, Bath, United Kingdom, 2019: pp. 14–18.

[48] C.D. Johnston, Fiber-reinforced cements and concretes, 1st ed., Taylor and Francis eLibrary, Abingdon - United Kingdom, 2010.

[49] S. Sharda, M. Singh, S. Singh, A review on Properties of Fiber Reinforced Cement-based materials, IOSR J. Mech. Civ. Eng. 13 (2016) 104–112. doi:10.9790/1684-130501104112.

[50] G.A. Hamdy, M.O.R. El-Hariri, M.F. Farag, Use of additives in mortar to enhance the compression and bond strength of masonry exposed to different environmental conditions, J. Build. Eng. 25 (2019) 100765. doi:10.1016/j.jobe.2019.100765.

[51] R. de S. Castoldi, L.M.S. de Souza, F. de Andrade Silva, Comparative study on the mechanical behavior and durability of polypropylene and sisal fiber reinforced concretes, Constr. Build. Mater. 211 (2019) 617– 628. doi:10.1016/j.conbuildmat.2019.03.282.

[52] A. Okeola, S. Abuodha, J. Mwero, Experimental Investigation of the Physical and Mechanical Properties of Sisal Fiber-Reinforced Concrete, Fibers. 6 (2018) 53. doi:10.3390/fib6030053.

[53] A. Neves e Sousa, M. Pedroso, National Patent INPI PT108169: Mat produced from cellulosic fibers, originated in Maritime pine needles, for thermal insulation and sound absorption, and its manufacturing process (in Portuguese), INPI PT108169, 2017.

[54] M. Pedroso, I. Flores-Colen, J.D. Silvestre, M.G. Gomes, Study on the thermal conductivity performance of cement-based composites incorporating natural organic fibres, in: R. Ball, B. Dams, V. Ferrandiz-Mas, X. Ke, K. Paine, M. Tyrer, P. Walker (Eds.), 39th Cem. Concr. Sci. Conf. 2019, University of Bath, Bath, United Kingdom, 2019: pp. 112–115.

[55] Enersens, Product data sheet: Aerogel kwark, (2019). http://enersens.fr/en/home/ (accessed January 7, 2020).

[56] Twaron, Product datasheet: Aramid roving 805 TEX, 2019.

[57] O. Onuaguluchi, N. Banthia, Plant-based natural fibre reinforced cement composites: A review, Cem. Concr. Compos. 68 (2016) 96–108. doi:10.1016/j.cemconcomp.2016.02.014.

[58] Saint-Gobain Weber, Technical datasheet: Webertherm pro (in Portuguese), 2019.

[59] A. Emdadi, I. Mehdipour, N.A. Libre, M. Shekarchi, Optimized workability and mechanical properties of FRCM by using fiber factor approach: theoretical and experimental study, Mater. Struct. 48 (2015) 1149–1161. doi:10.1617/s11527-013-0221-3.

[60] Y. Nakamura, Y. Ono, T. Saito, A. Isogai, Characterization of cellulose microfibrils, cellulose molecules, and hemicelluloses in buckwheat and rice husks, Cellulose. (2019). doi:10.1007/s10570-019-02560-4.

[61] P. Rebolledo, A. Cloutier, M.-C. Yemele, Effect of Density and Fiber Size on Porosity and Thermal Conductivity of Fiberboard Mats, Fibers. 6 (2018) 81. doi:10.3390/fib6040081.

[62] CEN, EN 1015-11: Methods of test for mortar for masonary - Part 11: Determination of flexural and compressive strength of hardened mortar, Comité Européen de Normalisation, Belgium, 1999.

[63] A.M. Brandt, Cement-Based Composites: Materials, Mechanical Properties and Performance, 2nd ed., Taylor and Francis, Abingdon - United Kingdom, 2009.

[64] P.K. Mehta, P.J.M. Monteiro, Concrete: Microstructure, properties and materials, 3rd ed., McGraw Hill Companies Inc, USA, 2006. doi:10.1036/0071462899.

[65] K. Arsène, M-A Savastano Jr, H. Allameh, S. M. Ghavami, W.O. Soboyejo, Cementitious composites reinforced with vegetable fibers, Proc. 1st Interam. Conf. Non-Conventional Mater. Technol. EcoConstruction Infrastruct. (2003) 13–16.

[66] L.A. Medina, J. Dzalto, 1.11 Natural Fibers, Compr. Compos. Mater. II. 1 (2017) 269–294. doi:10.1016/b978-0-12-803581-8.09877-5.

[67] J. Müssig, ed., Industrial Applications of Natural Fibres, 1st ed., John Wiley & Sons, Ltd, Chichester, UK, 2010. doi:10.1002/9780470660324.

[68] ASTM International, ASTM D792 - 13: Standard Test Methods for Density and Specific Gravity (Relative Density) of Plastics by Displacement, 2013. doi:10.1520/D0792-13.

[69] A. Célino, S. Fréour, F. Jacquemin, P. Casari, The hygroscopic behavior of plant fibers: a review, Front. Chem. 1 (2014) 1–12. doi:10.3389/fchem.2013.00043.

[70] Z. Saghrouni, D. Baillis, A. Jemni, Composites based on Juncus maritimus fibers for building insulation, Cem. Concr. Compos. 106 (2020) 103474. doi:10.1016/j.cemconcomp.2019.103474.

[71] CEN, EN 1015-6: Methods of test for mortar for masonry - Part 6: Determination of bulk density of fresh mortar, Comité Européen de Normalisation, Belgium, 1998.

[72] CEN, EN 1015-3: Methods of test for mortar for masonry - Part 3: Determination of consistence of fresh mortar (by flow table), Comité Européen de Normalisation, Belgium, 1999.

[73] CEN, EN 1015-7: Methods of test for mortar for masonry - Part 7 : Determination of air content of fresh mortar, Comité Européen de Normalisation, Belgium, 1998.

[74] CEN, EN 1015-10: Methods of test for mortar for masonry - Part 10: Determination of dry bulk density of hardened mortar, Comité Européen de Normalisation, Belgium, 1999.

[75] ASTME1876, ASTME1876: Standard Test Method for Dynamic Young's Modulus, Shear Modulus, and Poisson's Ratio by Impulse Excitation of Vibration, Annu. B. ASTM Stand. (2015) 1–15. doi:10.1520/E1876-09.

[76] CEN, EN 1015-12: Methods of test for mortar for masonry - Part 12: Determination of adhesive strength of hardened rendering and plastering mortars on substrates, Comité Européen de Normalisation, Belgium, 2000.

[77] I. Flores-Colen, J. de Brito, V. de Freitas, Expected render performance assessment based on impact resistance in situ determination, Constr. Build. Mater. 23 (2009) 2997–3004. doi:10.1016/j.conbuildmat.2009.05.003.

[78] LNEC, Test sheet - FE Pa 25: Wall coating. Sphere impact test (in Portuguese), Portugal, 1980.

[79] RILEM, RILEM MS-D7: Determination of pointing hardness by pendulum hammer, 1997.

[80] CEN, EN 1745: Masonry and masonry products — Methods for determining thermal properties, Comité Européen de Normalisation, Belgium, 2012.

[81] M.G. Gomes, I. Flores-Colen, L.M. Manga, A. Soares, J. de Brito, The influence of moisture content on the thermal conductivity of external thermal mortars, Constr. Build. Mater. 135 (2017) 279–286. doi:10.1016/j.conbuildmat.2016.12.166.

[82] M.G. Gomes, I. Flores-Colen, F. da Silva, M. Pedroso, Thermal conductivity measurement of thermal insulating mortars with EPS and silica aerogel by steady-state and transient methods, Constr. Build. Mater. 172 (2018) 696–705. doi:10.1016/j.conbuildmat.2018.03.162.

[83] American Society for Testing and Materials, ASTM D5334 - 14 - Standard Test Method for Determination of Thermal Conductivity of Soil and Soft Rock by Thermal Needle Probe Procedure, USA, 2014. doi:10.1520/D5334-14.

[84] American Society for Testing and Materials, ASTM D5930 - 17 - Standard Test Method for Thermal Conductivity of Plastics by Means of a Transient Line-Source Technique, USA, 2009. doi:10.1520/D593009.2.

[85] ISO/TC 61/SC 5, ISO 22007-2: 2015 - Plastics - Determination of thermal conductivity and thermal diffusivity - Part 2: Transient plane heat source (hot disc) method, ISO, Switzerland, 2015.

[86] ISO/TC 163/SC 2, ISO 10456: 2007 - Building materials and products - Hygrothermal properties - Tabulated design values and procedures for determining declared and design thermal values, ISO, Switzerland, 2007.

[87] Applied Precision Ltd., Isomet 2114 Thermal properties analyzer user's guide, Version 120712, Bratislava - Slovakia, 2019.

[88] CEN, EN 1015-18: Methods of test for mortar for masonry - Part 18: Determination of water absorption coefficient due to capillary action of hardened mortar, Comité Européen de Normalisation, Belgium, 2002.

[89] CEN, EN ISO 15148: Hygrothermal performance of building materials and products - Determination of water absorption coefficient by partial immersion, Comité Européen de Normalisation, Belgium, 2002.

[90] CEN, EN 16322: Conservation of cultural heritage - test methods - determination of drying properties, Comité Européen de Normalisation, Belgium, 2013.

[91] CEN, EN 1015-19 1998/A1: Methods of test for mortar for masonry - Part 19: Determination of water vapour permeability of hardened rendering and plastering mortars, 2004.

[92] CEN, EN ISO 12572: Hygrothermal performance of building materials and products. Determination of water vapour transmission properties, Comité Européen de Normalisation, Belgium, 2001.

[93] F. McGregor, A. Heath, E. Fodde, A. Shea, Conditions affecting the moisture buffering measurement performed on compressed earth blocks, Build. Environ. 75 (2014) 11–18. doi:10.1016/j.buildenv.2014.01.009.

[94] M. Palumbo, A.M. Lacasta, M.P. Giraldo, L. Haurie, E. Correal, Bio-based insulation materials and their hygrothermal performance in a building envelope system (ETICS), Energy Build. 174 (2018) 147–155. doi:10.1016/j.enbuild.2018.06.042.

[95] A.R. Santos, M. do R. Veiga, A. Santos Silva, J. de Brito, Microstructure as a critical factor of cement mortars' behaviour: The effect of aggregates' properties, Cem. Concr. Compos. 111 (2020) 103628. doi:10.1016/j.cemconcomp.2020.103628.

[96] K. Scrivener, A. Bazzoni, B. Mota, J. Rossen, Electron microscopy, in: K. Scrivener, R. Snellings, B. Lothenbach (Eds.), A Pract. Guid. to Microstruct. Anal. Cem. Mater., 1st ed., CRC press, Boca Raton, USA, 2016: pp. 351–418.

[97] K.S.W. Sing, D.H. Everett, R.A.W. Haul, L. Moscou, R.A. Pierotti, J. Rouquerol, T. Siemieniewska, Reporting physisorption data for gas/solid systems with special reference to the determination of surface area and porosity, Pure Appl. Chem. 57 (1985) 603–619. doi:10.1351/pac198557040603.

[98] E.W. Washburn, Note on a Method of Determining the Distribution of Pore Sizes in a Porous Material, Proc. Natl. Acad. Sci. U. S. A. 7 (1921) 115–6.

[99] Q. Zeng, K. Li, T. Fen-Chong, P. Dangla, Pore structure of cement pastes through NAD and MIP analysis, Adv. Cem. Res. 28 (2016) 23–32. doi:10.1680/adcr.14.00109.

[100] A. Kooshkaki, H. Eskandari-Naddaf, Effect of porosity on predicting compressive and flexural strength of cement mortar containing micro and nano-silica by multi-objective ANN modeling, Constr. Build. Mater. 212 (2019) 176–191. doi:10.1016/j.conbuildmat.2019.03.243.

[101] K.K. Aligizaki, Pore Structure of Cement-Based Materials, 1st ed., CRC Press, London - United Kingdom, 2005. doi:10.1201/9781482271959.

[102] S. Mindess, J.F. Young, D. Darwin, Concrete, 2nd ed., Prentice Hall, Englewood cliffs, NJ, 2002.

[103] E. Berodier, J. Bizzozero, A.C.A. Muller, Mercury intrusion porosimetry, in: K. Scrivener, R. Snellings, B. Lothenbach (Eds.), A Pract. Guid. to Microstruct. Anal. Cem. Mater., 1st ed., CRC press, Boca Raton, USA, 2016: pp. 419–444.

[104] D.N. Winslow, S. Diamond, A mercury porosimetry study of the evolution of porosity in Portland cement, J. Mater. 5 (1970) 564–585.

[105] Z. Liu, D. Winslow, Sub-distributions of pore size: A new approach to correlate pore structure with permeability, Cem. Concr. Res. 25 (1995) 769–778. doi:10.1016/0008-8846(95)00067-M.

[106] K. Nakamoto, Infrared and Raman Spectra of Inorganic and Coordination Compounds Part A : Theory and Applications, 6th ed., John Wiley & Sons, Inc., Hoboken, NJ, EUA, 2009.

[107] M. Derrick, D. Stulik, J.M. Landry, Infrared spectroscopy in conservation science: scientific tools for conservation, 1st ed., The Getty Conservation Institute, Los Angeles - USA, 1999.

[108] L. Fernández-Carrasco, D. Torrens-Martín, L.M. Morales, S. Martínez-Ramírez, Infrared Spectroscopy in the Analysis of Building and Construction Materials, in: T. Theophile (Ed.), Infrared Spectrosc. - Mater. Sci. Eng. Technol., InTech, 2012. doi:10.5772/36186.

[109] B. Smith, Infrared Spectral Interpretation: A System Approach, 1st ed., CRC press, Boca Raton, EUA, 1999.

[110] P. Larkin, Infrared and Raman spectroscopy: Principles and spectral interpretation, 1st ed., Elsevier, Oxford - United Kingdom, 2011.

[111] V. a. Alvarez, A. Vázquez, Influence of fiber chemical modification procedure on the mechanical properties and water absorption of MaterBi-Y/sisal fiber composites, Compos. Part A Appl. Sci. Manuf. 37 (2006) 1672–1680. doi:10.1016/j.compositesa.2005.10.005.

[112] E.M. Fernandes, J.F. Mano, R.L. Reis, Hybrid cork–polymer composites containing sisal fibre: Morphology, effect of the fibre treatment on the mechanical properties and tensile failure prediction, Compos. Struct. 105 (2013) 153–162. doi:10.1016/j.compstruct.2013.05.012.

[113] S.H. Chu, L.G. Li, A.K.H. Kwan, Fibre factors governing the fresh and hardened properties of steel FRC, Constr. Build. Mater. 186 (2018) 1228–1238. doi:10.1016/j.conbuildmat.2018.08.047.

[114] D.-Y. Yoo, S. Kim, G.-J. Park, J.-J. Park, S.-W. Kim, Effects of fiber shape, aspect ratio, and volume fraction on flexural behavior of ultra-high-performance fiber-reinforced cement composites, Compos. Struct. 174 (2017) 375–388. doi:10.1016/j.compstruct.2017.04.069.

[115] DuPont, Kevlar technical guide, 1990.

[116] E. Guyer, D. Brownell, eds., Handbook of Applied Thermal Design, 1st ed., Taylor & Francis, Philadelphia - USA, 1999.

[117] J. Wei, S. Ma, D.G. Thomas, Correlation between hydration of cement and durability of natural fiberreinforced cement composites, Corros. Sci. 106 (2016) 1–15. doi:10.1016/j.corsci.2016.01.020.

[118] V. Agopyan, H. Savastano, V.M. John, M.A. Cincotto, Developments on vegetable fibre–cement based materials in São Paulo, Brazil: an overview, Cem. Concr. Compos. 27 (2005) 527–536. doi:10.1016/j.cemconcomp.2004.09.004.

[119] P.R.L. Lima, H.M. Santos, G.P. Camilloto, R.S. Cruz, Effect of Surface Biopolymeric Treatment on Sisal Fiber Properties and Fiber-Cement Bond, J. Eng. Fiber. Fabr. 12 (2017) 155892501701200. doi:10.1177/155892501701200207.

[120] N. Benmansour, B. Agoudjil, A. Gherabli, A. Kareche, A. Boudenne, Thermal and mechanical performance of natural mortar reinforced with date palm fibers for use as insulating materials in building, Energy Build. 81 (2014) 98–104. doi:10.1016/j.enbuild.2014.05.032.

[121] F. Pacheco-Torgal, S. Jalali, Cementitious building materials reinforced with vegetable fibres: A review, Constr. Build. Mater. 25 (2011) 575–581. doi:10.1016/j.conbuildmat.2010.07.024.

[122] M. Ibrahim, P.H. Biwole, P. Achard, E. Wurtz, G. Ansart, Building envelope with a new aerogel-based insulating rendering: Experimental and numerical study, cost analysis, and thickness optimization, Appl. Energy. 159 (2015) 490–501. doi:10.1016/j.apenergy.2015.08.090.

[123] M. Ibrahim, P.H. Biwole, P. Achard, E. Wurtz, Aerogel-Based Materials for Improving the Building Envelope's Thermal Behavior: A Brief Review with a Focus on a New Aerogel-Based Rendering, in: A. Sharma, S.K. Kar (Eds.), Energy Sustain. Trough Green Energy, Green Energy Technol., Springer India, 2015: pp. 163–188. doi:10.1007/978-81-322-2337-5_7.

[124] J.F. Maia, Durability of Thermal Rendering and Plastering Systems, University of Porto, 2019.

[125] A. Badache, A.S. Benosman, Y. Senhadji, M. Mouli, Thermo-physical and mechanical characteristics of sand-based lightweight composite mortars with recycled high-density polyethylene (HDPE), Constr. Build. Mater. 163 (2018) 40–52. doi:10.1016/j.conbuildmat.2017.12.069.

[126] B. Abu-Jdayil, A.-H. Mourad, W. Hittini, M. Hassan, S. Hameedi, Traditional, state-of-the-art and renewable thermal building insulation materials: An overview, Constr. Build. Mater. 214 (2019) 709–735. doi:10.1016/j.conbuildmat.2019.04.102.

[127] H.-P. Ebert, Thermal Properties of Aerogels, in: M. Aegerter, N. Leventis, M.M. Koebel (Eds.), Aerogels Handb., 1st ed., Springer New York, New York, NY, 2011: pp. 537–564. doi:10.1007/978-1-4419-75898_23.

[128] A.E. Richardson, Freeze/thaw durability in concrete with fibre additions, Struct. Surv. 21 (2003) 225–233. doi:10.1108/02630800310511569.

[129] M. Karoglou, A. Moropoulou, Z.B. Maroulis, M.K. Krokida, Drying Kinetics of Some Building Materials, Dry. Technol. 23 (2005) 305–315. doi:10.1081/DRT-200047926.

[130] C. Hall, W.D. Hoff, Water Transport in Brick, Stone and Concrete, 2nd ed., CRC Press, Boca Raton, USA, 2009.

[131] A. Isebaert, W. De Boever, F. Descamps, J. Dils, M. Dumon, G. De Schutter, E. Van Ranst, V. Cnudde, L. Van Parys, Pore-related properties of natural hydraulic lime mortars: an experimental study, Mater. Struct. 49 (2016) 2767–2780. doi:10.1617/s11527-015-0684-5.

[132] P. Faria, T. Santos, J.-E. Aubert, Experimental Characterization of an Earth Eco-Efficient Plastering Mortar, J. Mater. Civ. Eng. 28 (2016) 04015085. doi:10.1061/(ASCE)MT.1943-5533.0001363.

[133] M.I. Gomes, T.D. Gonçalves, P. Faria, Earth-based repair mortars: Experimental analysis with different binders and natural fibers, Rammed Earth Conserv. (2012) 661–668.

[134] M.C. de F. Salomão, E. Bauer, C. de S. Kazmierczak, Drying parameters of rendering mortars, Ambient. Construído. 18 (2018) 7–19. doi:10.1590/s1678-86212018000200239.

[135] C. Buratti, E. Belloni, F. Merli, Water vapour permeability of innovative building materials from different waste, Mater. Lett. 265 (2020) 127459. doi:10.1016/j.matlet.2020.127459.

[136] J. Válek, J. Hughes, P. Bartos, Gas Permeability, Porosity and Carbonation of Modern Conservation Lime Mortar Mix, in: Mater. Build. Struct., Wiley-VCH Verlag GmbH & Co. KGaA, Weinheim, FRG, 2005: pp. 209–215. doi:10.1002/3527606211.ch30.

[137] S. Fantucci, E. Fenoglio, V. Serra, M. Perino, M. Dutto, V. Marino, Hygrothermal Characterization of High-Performance Aerogel-Based Internal Plaster, in: J. Littlewood, R. Howlett, A. Capozzoli, L. Jain (Eds.), Sustain. Energy Build. Smart Innov. Syst. Technol., 1st ed., Springer, Singapore, 2020: pp. 259– 268. doi:10.1007/978-981-32-9868-2_22.

[138] M. Ibrahim, E. Wurtz, P.H. Biwole, P. Achard, H. Sallee, Hygrothermal performance of exterior walls covered with aerogel-based insulating rendering, Energy Build. 84 (2014) 241–251. doi:10.1016/j.enbuild.2014.07.039.

[139] L. Ducoulombier, Z. Lafhaj, Comparative study of hygrothermal properties of five thermal insulation materials, Case Stud. Therm. Eng. 10 (2017) 628–640. doi:10.1016/j.csite.2017.11.005.

[140] C. Hill, M. Hughes, Natural Fibre Reinforced Composites Opportunities and Challenges, J. Biobased Mater. Bioenergy. 4 (2010) 148–158. doi:10.1166/jbmb.2010.1079.

[141] M.P. Ansell, R.J. Ball, M. Lawrence, D. Maskell, A. Shea, P. Walker, Green composites for the built environment, in: Green Compos., Elsevier, 2017: pp. 123–148. doi:10.1016/B978-0-08-100783-9.00006X.

[142] Y. Xie, C.A.S. Hill, Z. Jalaludin, S.F. Curling, R.D. Anandjiwala, A.J. Norton, G. Newman, The dynamic water vapour sorption behaviour of natural fibres and kinetic analysis using the parallel exponential kinetics model, J. Mater. Sci. 46 (2011) 479–489. doi:10.1007/s10853-010-4935-0.

[143] M. Fukuda, M. Ochi, M. Miyagawa, H. Kawai, Moisture Sorption Mechanism of Aromatic Polyamide Fibers: Stoichiometry of the Water Sorbed in Poly(para-phenylene Terephthalamide) Fibers1, Text. Res. J. 61 (1991) 668–680. doi:10.1177/004051759106101107.

[144] D.A. Mooney, J.M.D. MacElroy, Differential Water Sorption Studies on Kevlar 49 and As-Polymerized Poly(p -phenylene terephthalamide): Determination of Water Transport Properties, Langmuir. 23 (2007) 11804–11811. doi:10.1021/la7017538.

[145] A. Kicińska-Jakubowska, E. Bogacz, M. Zimniewska, Review of Natural Fibers. Part I—Vegetable Fibers, J. Nat. Fibers. 9 (2012) 150–167. doi:10.1080/15440478.2012.703370.

[146] R.A. Cook, K.C. Hover, Mercury porosimetry of hardened cement pastes, Cem. Concr. Res. 29 (1999) 933–943. doi:10.1016/S0008-8846(99)00083-6.

[147] N. Hearn, R.D. Hooton, Sample mass and dimension effects on mercury intrusion porosimetry results, Cem. Concr. Res. 22 (1992) 970–980. doi:10.1016/0008-8846(92)90121-B.

[148] J. van Brakel, S. Modry, M. Svatá, Mercury porosimetry: state of the art, Powder Technol. 29 (1981) 1– 12. doi:10.1016/S0422-9894(08)70338-6.

[149] M. Ternan, L.P. Mysak, Hysteresis caused by dimensional changes of porous solids during mercury porosimetry, Powder Technol. 52 (1987) 29–34. doi:10.1016/0032-5910(87)80004-9.

[150] X. Wang, Y. Peng, J. Wang, Q. Zeng, Pore Structure Damages in Cement-Based Materials by Mercury Intrusion: A Non-Destructive Assessment by X-Ray Computed Tomography, Materials (Basel). 12 (2019) 2220. doi:10.3390/ma12142220.

[151] M. de Fátima Júlio, A. Soares, L.M. Ilharco, I. Flores-Colen, J. de Brito, Aerogel-based renders with lightweight aggregates: Correlation between molecular/pore structure and performance, Constr. Build. Mater. 124 (2016) 485–495. doi:10.1016/j.conbuildmat.2016.07.103.

[152] F. Rouquerol, J. Rouquerol, K. Sing, Assessment of Mesoporosity, in: Adsorpt. by Powders Porous Solids, Elsevier, 1999: pp. 191–217. doi:10.1016/B978-012598920-6/50008-7.

[153] K.S.W. Sing, D.H. Everett, R.A.W. Haul, L. Moscou, R.A. Pierotti, J. Rouquerol, T. Siemieniewska, Reporting Physisorption Data for Gas/Solid Systems, in: Handb. Heterog. Catal., Wiley-VCH Verlag GmbH & Co. KGaA, Weinheim, Germany, 2008. doi:10.1002/9783527610044.hetcat0065.

[154] O.-J. Lee, K.-H. Lee, T. Jin Yim, S. Young Kim, K.-P. Yoo, Determination of mesopore size of aerogels from thermal conductivity measurements, J. Non. Cryst. Solids. 298 (2002) 287–292. doi:10.1016/S00223093(01)01041-9.

[155] U. Berardi, Aerogel-enhanced insulation for building applications, in: F. Pacheco-Torgal, M. Diamantini, A. Nazari, C. Goran-Granqvist, A. Pruna, S. Amirkhanian (Eds.), Nanotechnol. Eco-Efficient Constr., 2nd ed., Woodhead Publishing Ltd, UK, 2019: pp. 395–416. doi:10.1016/B978-0-08-102641-0.00017-7.

[156] M. Koebel, A. Rigacci, P. Achard, Aerogel-based thermal superinsulation: an overview, J. Sol-Gel Sci. Technol. 63 (2012) 315–339. doi:10.1007/s10971-012-2792-9.

[157] M.A. Aegerter, N. Leventis, M.M. Koebel, eds., Aerogels Handbook, Springer New York, New York, NY, 2011. doi:10.1007/978-1-4419-7589-8.

[158] K. Scrivener, R. Snellings, B. Lothenbach, eds., A practical guide to microstructural analysis of cementitious materials, 1st ed., CRC press, Boca Raton, EUA, 2016.

[159] S.R. Ferreira, M. Pepe, E. Martinelli, F. de Andrade Silva, R.D. Toledo Filho, Influence of natural fibers characteristics on the interface mechanics with cement based matrices, Compos. Part B Eng. 140 (2018) 183–196. doi:10.1016/j.compositesb.2017.12.016.

[160] S. Pérez, K. Mazeau, Conformations, structures and morphologies of celluloses, in: S. Dumitriu (Ed.), Polysaccharides Struct. Divers. Funct. Versatility, 2nd ed., Marcel Dekker, 2005: pp. 41–68.

[161] J. Coates, Interpretation of Infrared Spectra, A Practical Approach, in: R.A. Meyers (Ed.), Encycl. Anal. Chem., 1st ed., John Wiley & Sons, Inc., Hoboken, NJ, EUA, 2004: pp. 1–23.

[162] J. Lambert, H. Shurvell, R. Cooks, L. Verbit, Introduction to Organic Spectroscopy, 1st ed., Macmillan, 1987.

[163] P. Yu, R.J. Kirkpatrick, B. Poe, P.F. McMillan, X. Cong, Structure of Calcium Silicate Hydrate (C-S-H): Near-, Mid-, and Far-Infrared Spectroscopy, J. Am. Ceram. Soc. 82 (2004) 742–748. doi:10.1111/j.11512916.1999.tb01826.x.

[164] S.N. Ghosh, A.K. Chatterjee, Absorption and reflection infra-red spectra of major cement minerals, clinkers and cements, J. Mater. Sci. 9 (1974) 1577–1584. doi:10.1007/BF00540754.

[165] J. Bensted, Uses of Raman Spectroscopy in Cement Chemistry, J. Am. Ceram. Soc. 59 (1976) 140–143. doi:10.1111/j.1151-2916.1976.tb09451.x.

[166] S.N. Ghosh, S.K. Handoo, Infrared and Raman spectral studies in cement and concrete (review), Cem. Concr. Res. 10 (1980) 771–782. doi:10.1016/0008-8846(80)90005-8.

[167] P. Innocenzi, Infrared spectroscopy of sol–gel derived silica-based films: a spectra-microstructure overview, J. Non. Cryst. Solids. 316 (2003) 309–319.

[168] J. Cruz, R. Fangueiro, Surface Modification of Natural Fibers: A Review, Procedia Eng. 155 (2016) 285– 288. doi:10.1016/j.proeng.2016.08.030.

[169] L.G. Li, S.H. Chu, K.L. Zeng, J. Zhu, A.K.H. Kwan, Roles of water film thickness and fibre factor in workability of polypropylene fibre reinforced mortar, Cem. Concr. Compos. 93 (2018) 196–204. doi:10.1016/j.cemconcomp.2018.07.014.

[170] S. Ng, B.P. Jelle, L.I.C. Sandberg, T. Gao, Ó.H. Wallevik, Experimental investigations of aerogelincorporated ultra-high performance concrete, Constr. Build. Mater. 77 (2015) 307–316. doi:10.1016/j.conbuildmat.2014.12.064.

[171] J. Hu, Z. Ge, K. Wang, Influence of cement fineness and water-to-cement ratio on mortar early-age heat of hydration and set times, Constr. Build. Mater. 50 (2014) 657–663. doi:10.1016/j.conbuildmat.2013.10.011.

[172] J. Silva, J. de Brito, R. Veiga, Incorporation of fine ceramics in mortars, Constr. Build. Mater. 23 (2009) 556–564. doi:10.1016/j.conbuildmat.2007.10.014.

[173] A. Kareche, B. Agoudjil, B. Haba, A. Boudenne, Study on the Durability of New Construction Materials Based on Mortar Reinforced with Date Palm Fibers Wastes, Waste and Biomass Valorization. (2019). doi:10.1007/s12649-019-00669-y.

[174] T. Stahl, K. Ghazi Wakili, S. Hartmeier, E. Franov, W. Niederberger, M. Zimmermann, Temperature and moisture evolution beneath an aerogel based rendering applied to a historic building, J. Build. Eng. 12 (2017) 140–146. doi:10.1016/j.jobe.2017.05.016.

[175] J. Zhang, B. Chen, F. Yu, Preparation of EPS-Based Thermal Insulation Mortar with Improved Thermal and Mechanical Properties, J. Mater. Civ. Eng. 31 (2019) 04019183. doi:10.1061/(ASCE)MT.19435533.0002825.

[176] M. Boutarfa, R. Belouettar, A. Makradi, Comparative Study of Cement Mortar Reinforced with Vegetable Fibers Alfa , Date Palm and Diss: Mechanical Properties and Shrinkage, J. Mater. Environ. Sci. 9 (2018) 2304–2314.

[177] I. Flores-Colen, PhD Thesis in Civil Engineering: "Performance evaluation methodology for towed façades, from the perspective of predictive maintenance" (in Portuguese), University of Lisbon, 2009.

[178] B. Çomak, A. Bideci, Ö. Salli Bideci, Effects of hemp fibers on characteristics of cement based mortar, Constr. Build. Mater. 169 (2018) 794–799. doi:10.1016/j.conbuildmat.2018.03.029.

[179] J. Broda, Application of Polypropylene Fibrillated Fibres for Reinforcement of Concrete and Cement Mortars, in: S. Yilmaz, H. Ozmen (Eds.), High Perform. Concr. Technol. Appl., 1st ed., InTechOpen, 2016: pp. 189–204. doi:10.5772/64386.

[180] S. Kalia, A. Dufresne, B.M. Cherian, B.S. Kaith, L. Avérous, J. Njuguna, E. Nassiopoulos, CelluloseBased Bio- and Nanocomposites: A Review, Int. J. Polym. Sci. 2011 (2011) 1–35. doi:10.1155/2011/837875.

[181] C. Shi, J. Wang, P. Chen, J. Feng, J. Cui, F. Yang, Effects of oxygen plasma treatment on domestic aramid fiber III reinforced bismaleimide composite interfacial properties, IOP Conf. Ser. Mater. Sci. Eng. 274 (2017) 012104. doi:10.1088/1757-899X/274/1/012104.

[182] H. Savastano, P. Warden, R.S. Coutts, Brazilian waste fibres as reinforcement for cement-based composites, Cem. Concr. Compos. 22 (2000) 379–384. doi:10.1016/S0958-9465(00)00034-2.

[183] A. Hanif, S. Diao, Z. Lu, T. Fan, Z. Li, Green lightweight cementitious composite incorporating aerogels and fly ash cenospheres – Mechanical and thermal insulating properties, Constr. Build. Mater. 116 (2016) 422–430. doi:10.1016/j.conbuildmat.2016.04.134.

[184] R. Vatjai, Science and Engineering of Nanomaterials, in: R. Vatjai (Ed.), Springer Handb. Nanomater., 1st ed., Springer, Berlin, 2013: pp. 1–36.

[185] R.S.P. Coutts, Wood fiber reinforced cement composites, in: R.N. Swamy (Ed.), Nat. Fiber Reinf. Cem. Concr., 1st ed., Blackie academic and professional, Glasgow, 1988: pp. 208–242.

[186] S.F. Santos, R.S. Teixeira, H. Savastano Junior, Interfacial transition zone between lignocellulosic fiber and matrix in cement-based composites, in: Sustain. Nonconv. Constr. Mater. Using Inorg. Bond. Fiber Compos., Elsevier, 2017: pp. 27–68. doi:10.1016/B978-0-08-102001-2.00003-6.

[187] C.G. Hoyos, R. Zuluaga, P. Gañán, T.M. Pique, A. Vazquez, Cellulose nanofibrils extracted from fique fibers as bio-based cement additive, J. Clean. Prod. 235 (2019) 1540–1548. doi:10.1016/j.jclepro.2019.06.292.

[188] H.F.W. Taylor, Cement Chemistry, 2nd ed., Thomas Telford Publishing, London - United Kingdom, 1998. doi:10.1142/9781860949982_0010.

[189] P.C. Hewlett, ed., Lea's Chemistry of Cement and Concrete, 4th ed., Elsevier, Oxford - United Kingdom, 2004. doi:10.1016/B978-0-7506-6256-7.50031-X.

[190] L. Jiao, M. Su, L. Chen, Y. Wang, H. Zhu, H. Dai, Natural Cellulose Nanofibers As Sustainable Enhancers in Construction Cement, PLoS One. 11 (2016) e0168422. doi:10.1371/journal.pone.0168422.